Ultralight aerogels via supramolecular polymerization of a new chiral perfluoropyridin-based sulfonimidamide organogelator

Giampiero Proietti, [a] Anton Axelsson,[a] Antonio Capezza,[b] Yogesh Todarwal[c], Julius Kuzmin,[a] Mathieu Linares,[c, d] Patrick Norman[c], Zoltán Szabó,[a] Christofer Lendel,[a] Richard Olsson[b] and Peter Dinér*[a]

[a]*Department of Chemistry*
KTH Royal Institute of Technology
Teknikringen 30, 10044 Stockholm (Sweden).
E-mail: diner@kth.se

[b]*Department of Fibre and Polymer Technology*
KTH Royal Institute of Technology
Teknikringen 30, 10044 Stockholm (Sweden).

[d]*Department of Physics, Chemistry and Biology (IFM), Linköping University (Sweden)*

Table of Contents

Rheology

The test was performed using a DHR-2 Rheometer (TA Instruments, USA) using 25 mm diameter stainless steel parallel plates. The material was taken from the gel fraction of the samples, and the tests were performed at 25 °C. The gels were first subjected to an amplitude sweep (frequency = 1 Hz) from 1 e^{-4} 1 to e^{-7} MPa. A stress value from the linear region of the amplitude sweep was used in the frequency sweep test. The samples were then subjected to a frequency sweep from 1 e^{-3} to 100 Hz.

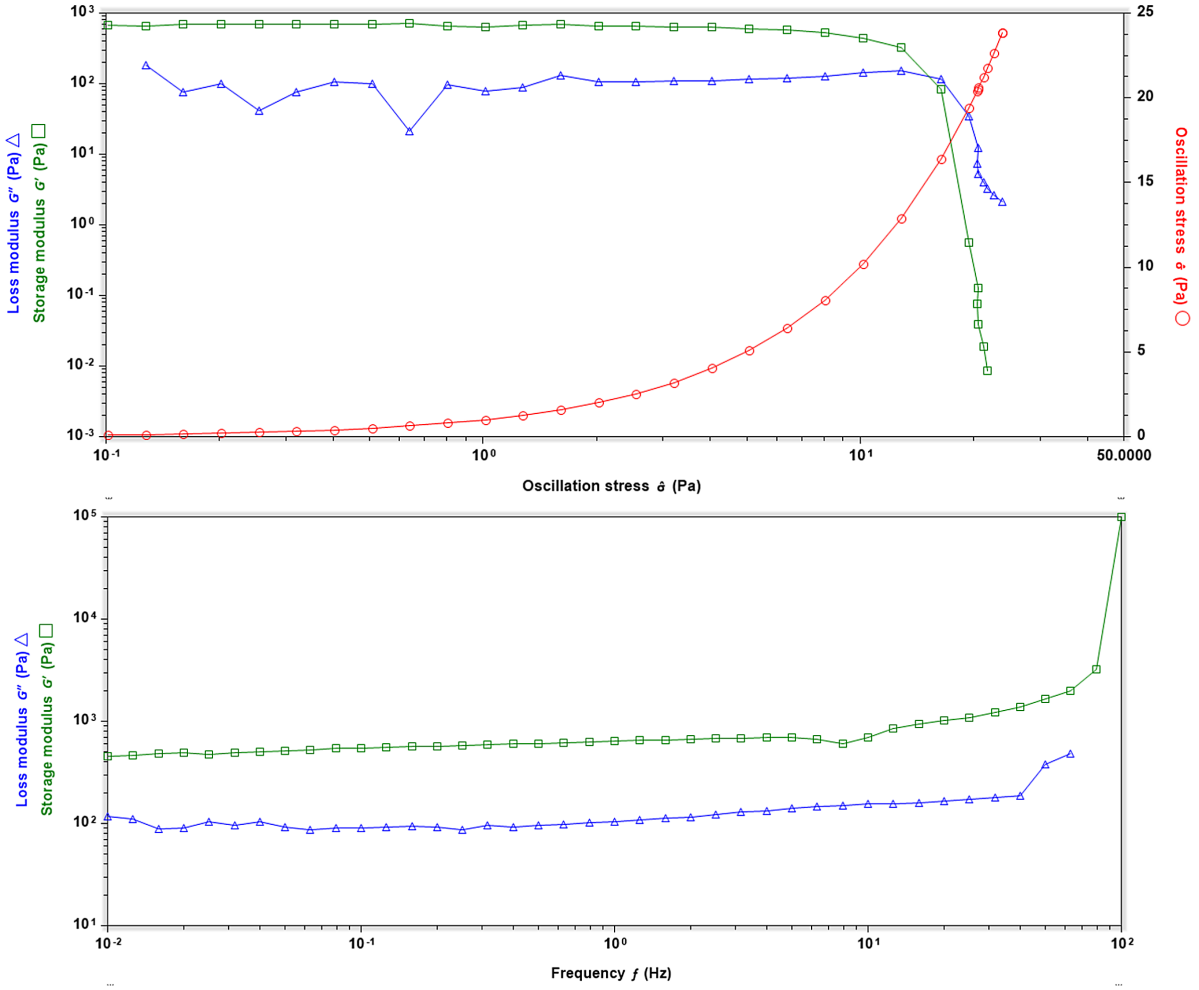

Figure S1. A) Full sweep Storage (green) and loss (blue) moduli of (*S*)-SIA (0.9 mg/mL) in heptane as a function of frequency. The frequency sweep was performed at a strain of 3 e^{-6} MPa (accordingly within the linear region from the amplitude sweep test) and T= 293 K.

General procedure for test of organogelator

The gelating abilities were tested via vial inversion test for in different solvents. The organogelator was added to a vial together with indicated solvent (0.25 ml, 0.125 M)). The gelator-solvent mixture was heated in an oil bath (110 °C) for ca 30 seconds or until the organogelator was completely dissolved and the solution was homogenous. The vial was then left to cool down at room temperature and the gelating abilities was tested via vial inversion. If a gel was formed and survived the vial inversion test, the concentration was reduced to half by addition of more solvent, the vial was heated and the procedure was repeated until no gel was formed.

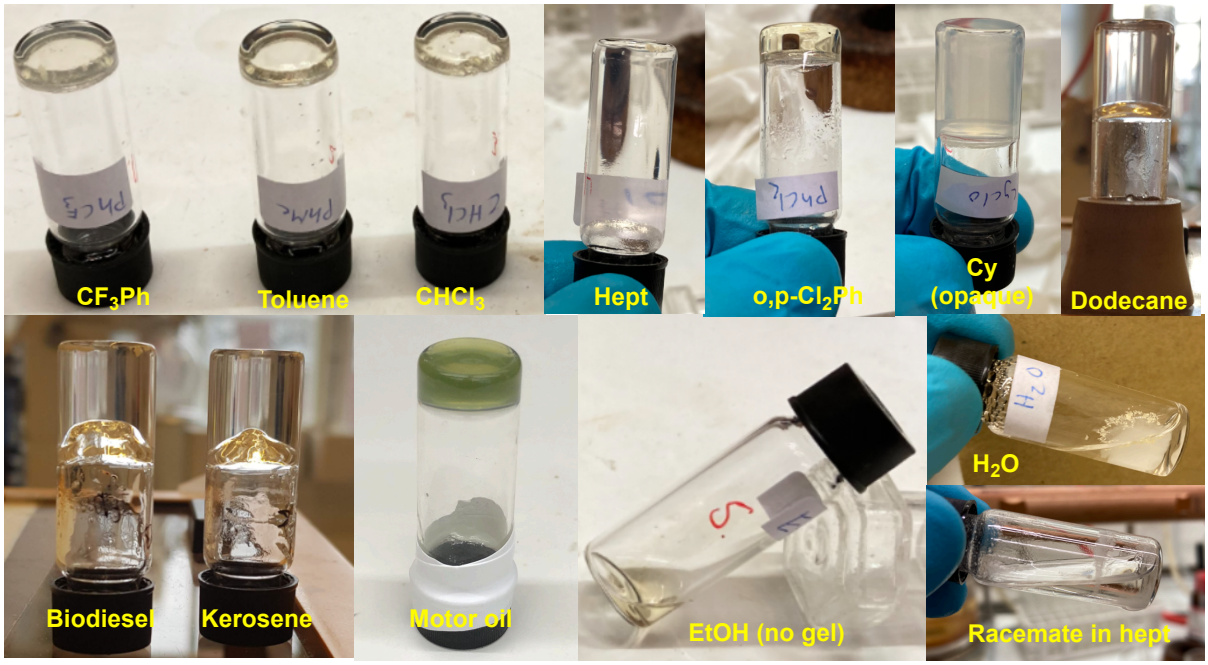

Figure S2. Examples of gelation of (*S*)-SIA in different solvents (CF_3Ph, toluene, chloroform, heptane, o,p-dichlorobenzene, cyclohexane (high concentration, opaque), docecane, Biodiesel (NextBTL), kerosene, motor oil), EtOH (no gel), water (precipitate), racemate of SIA (precipitate).

Nongelating SIA

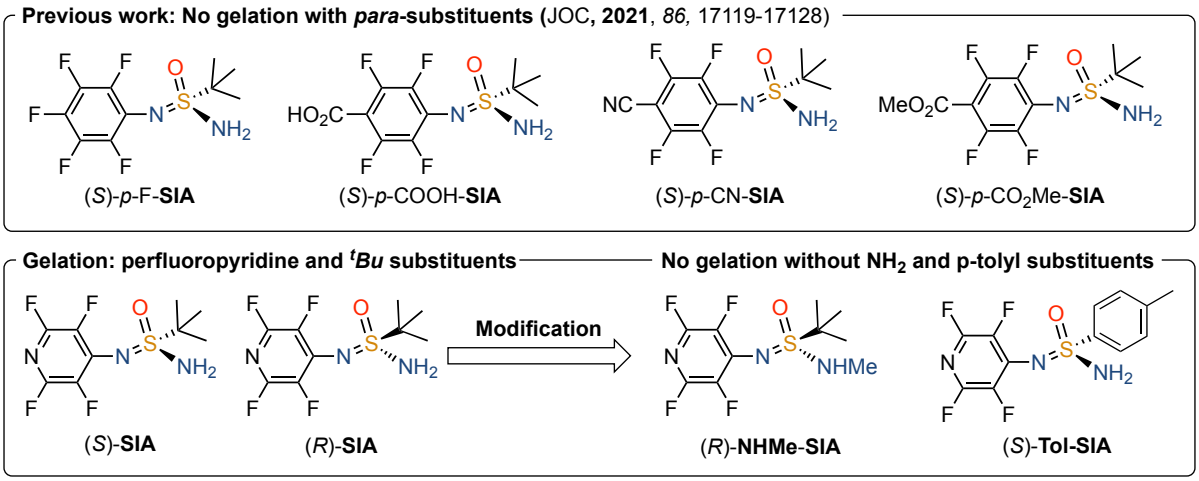

Figure S3. Nongelating sulfonimidamides from previous and current work.

Synthesis of nongelating SIA

*Synthesis of (R)-**NHMe-SIA***

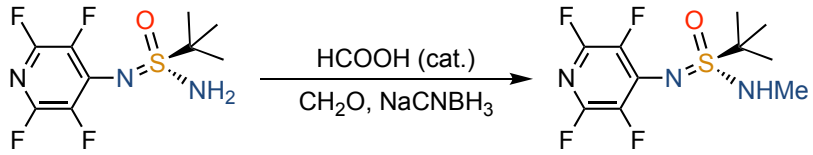

(*R*)-**SIA** (*R*)-**NHMe-SIA**

To a vial with (*R*)-**SIA** (42 mg, 0.15 mmol) and aqueous formaldehyde (22.5 ul, 0.30 mmol) was added an aqueous solution of formic acid (2 drops, 0.1 M) The solution was stirred for 1 hour. Sodium cyanoborohydride (21 mg, 0.32 mmol) was added and the reaction was stirred for 72 hours. The reaction mixture was diluted with dichloromethane (10 ml) and was washed with saturated Na_2CO_3 (3 · 10 ml). The organic phase was dried over $MgSO_4$ and the solvent was evaporated. The crude product was purified via preparative TLC using petroleum ether, dichloromethane and ethylacetate as an eluent (4:1:1) and the product was obtained as a white solid (21 mg, 47%).

^{1}H NMR ($CDCl_3$, 400 MHz): δ 4.08 (s, 1H, N*H*CH_3); 2.90 (d, 3H, NHC*H*$_3$); 1.54 (s, 9H, C(CH_3)$_3$ ^{13}C{^{1}H} NMR ($CDCl_3$, 125 MHz): δ 144.0 (m), 137.0 (m), 136.5 (m), 63.4, 31.4, 24.6; ^{19}F NMR ($CDCl_3$, 376 MHz): δ -152.2 (m, 2F), -93.7.9 (m, 2F). HRMS (ESI-TOF, *m/z*): calcd for $C_{10}H_{13}F_4N_3OS$ [M + H]$^+$, 300.0788; found, 300.0781.

*Synthesis of (S)-p-**Tol-SIA***

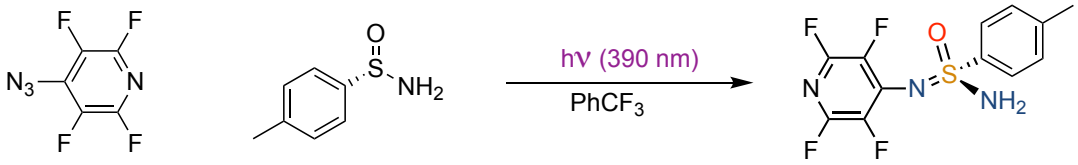

(*S*)-*p*-**Tol-SIA**

4-azido-2,3,5,6-tetrafluoropyridine (0.3 mmol, 0.05 M), (*S*)-4-methylbenzenesulfinamide (1.5 equiv, 0.45 mmol) were added together with degassed α,α,α-trifluorotoluene (6 mL). The vial was capped with a rubber septum and evacuated and backfilled with N_2. The reaction mixture was irradiated at 390 nm (40 W, Kessil PR160, maximum intensity, 3.0 cm from the reaction vessel) while stirring. After completion of the reaction, the crude obtained upon solvent removal under reduced pressure was purified by flash column chromatography using ether, dichloromethane and ethyl acetate (8:1:1) as the eluent system to afford the pure product (16 mg, 20%).

^{1}H NMR (MeOD-d_4, 400 MHz): δ 7.96 (d, 2H, J = 2.4 Hz); 7.42 (d, 2H, J = 2.4 Hz); 4.92 (s, 2H, NH_2), 2.45 (s, 3H, PhCH_3); ^{13}C{^{1}H} NMR (MeOD-d_4, 125 MHz): δ 144.6 (m), 143.7, 140.0, 137.1 (m), 136.8 (m), 129.3, 126.5, 20.o; ^{19}F NMR ($CDCl_3$, 376 MHz): δ -151.0 (m, 2F), -93.7 (m, 2F). HRMS (ESI-TOF, *m/z*): calcd for $C_{12}H_9F_4N_3OS$ [M + H]$^+$, 320.0475; found, 320.0458.

Scanning electron microscopy

Sample preparation: Xerogel samples were prepared by slow evaporation of solvent from the vial at room temperature. Aerogels samples were from the organogel in cyclohexane and were prepared by freezing and freeze-drying off the solvent under reduced pressure and temperature using a VirTis BenchTop Pro with Omnitronics.

SEM-analysis: The surface morphology was analyzed using a Hitachi S-4800 field emission scanning electron microscope (FE-SEM). A voltage of 3 kV and a current of 10 μA were used. The lyophilized materials were sputtered with a palladium/platinum (Pt/Pd) target in an Agar High Resolution Sputter Coater (model 208RH). The sputtering time for all samples was 45 s proving an estimated conductive layer of 1–2 nm.

Xerogel from (S)-SIA in heptane and $PhCF_3$

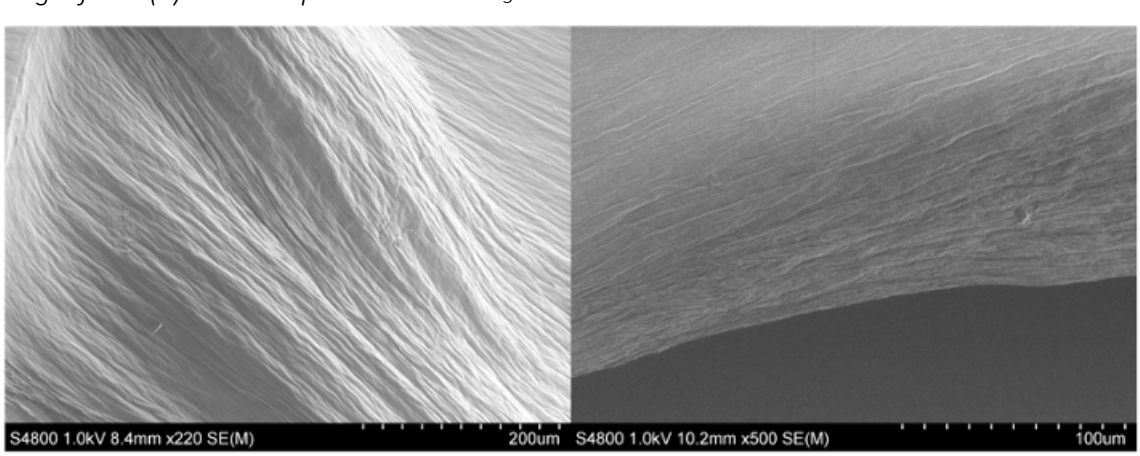

Figure S4. Air-dried xerogel from (*S*)-SIA (1 mg/mL) in heptane and $PhCF_3$.

Comparison of macroscopic helicity in xerogels from (S)-SIA and (R)-SIA

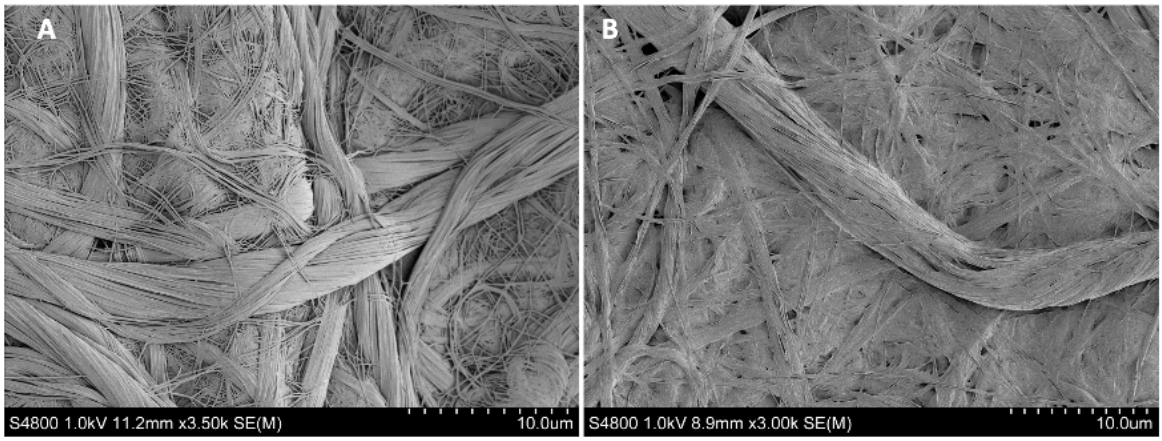

Figure S5. Comparison of (*S*)-SIA and (*R*)-SIA. (A) Air-dried xerogel from (*S*)-SIA in chloroform (14 mg/mL). B) Air-dried xerogel from (*R*)-SIA in chloroform (14 mg/mL)

Freeze-dried aerogel of (R)-SIA from cyclohexane

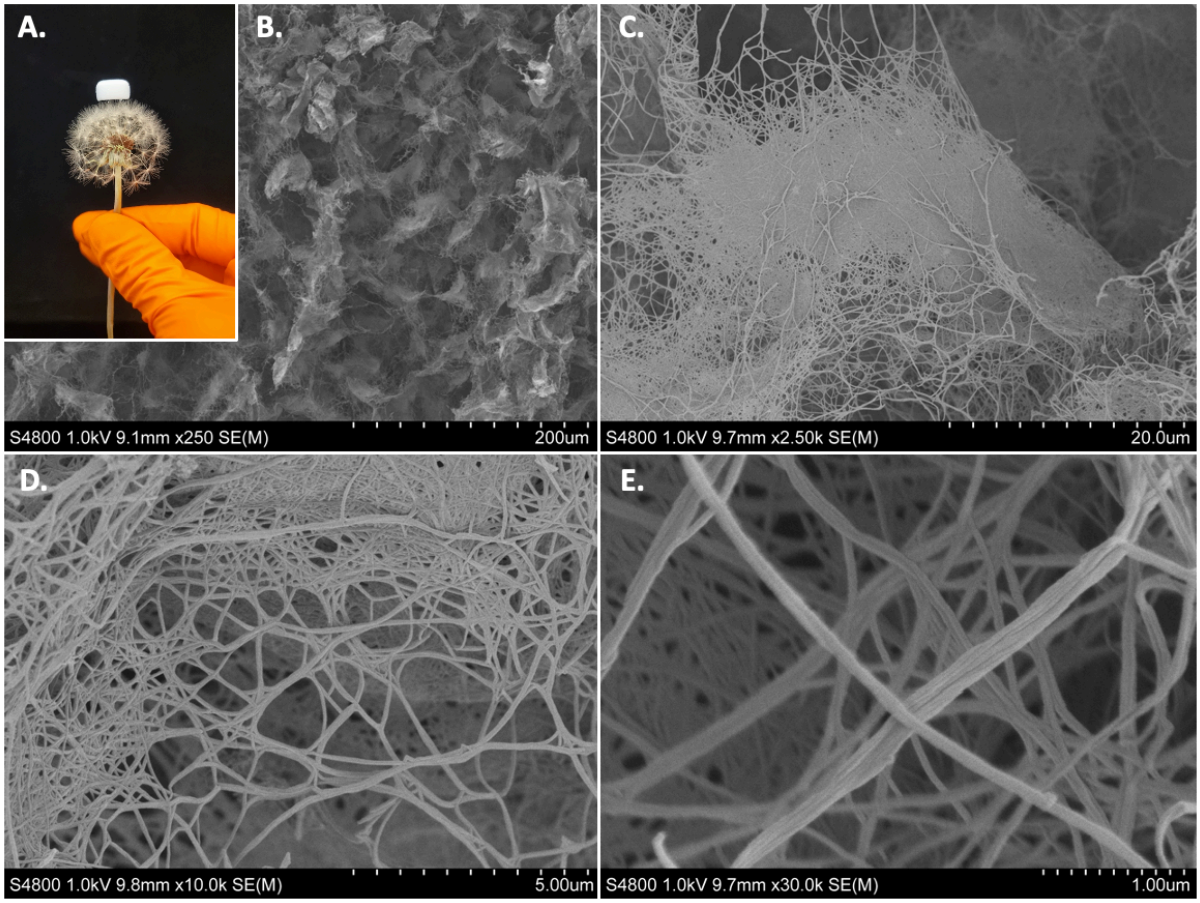

Figure S6. Enlarged picture of aerogel of (*R*)-**SIA** from cyclohexane. (A) Freeze-dried aerogel of (*R*)-**SIA** from cyclohexane resting on the seed head of a dandelion. (B) Top view of porous aerogel. (C) & (D) View of fibrous network of aerogel. (E) Individual fibres in the network.

Freeze-dried aerogel of (S)-SIA from cyclohexane

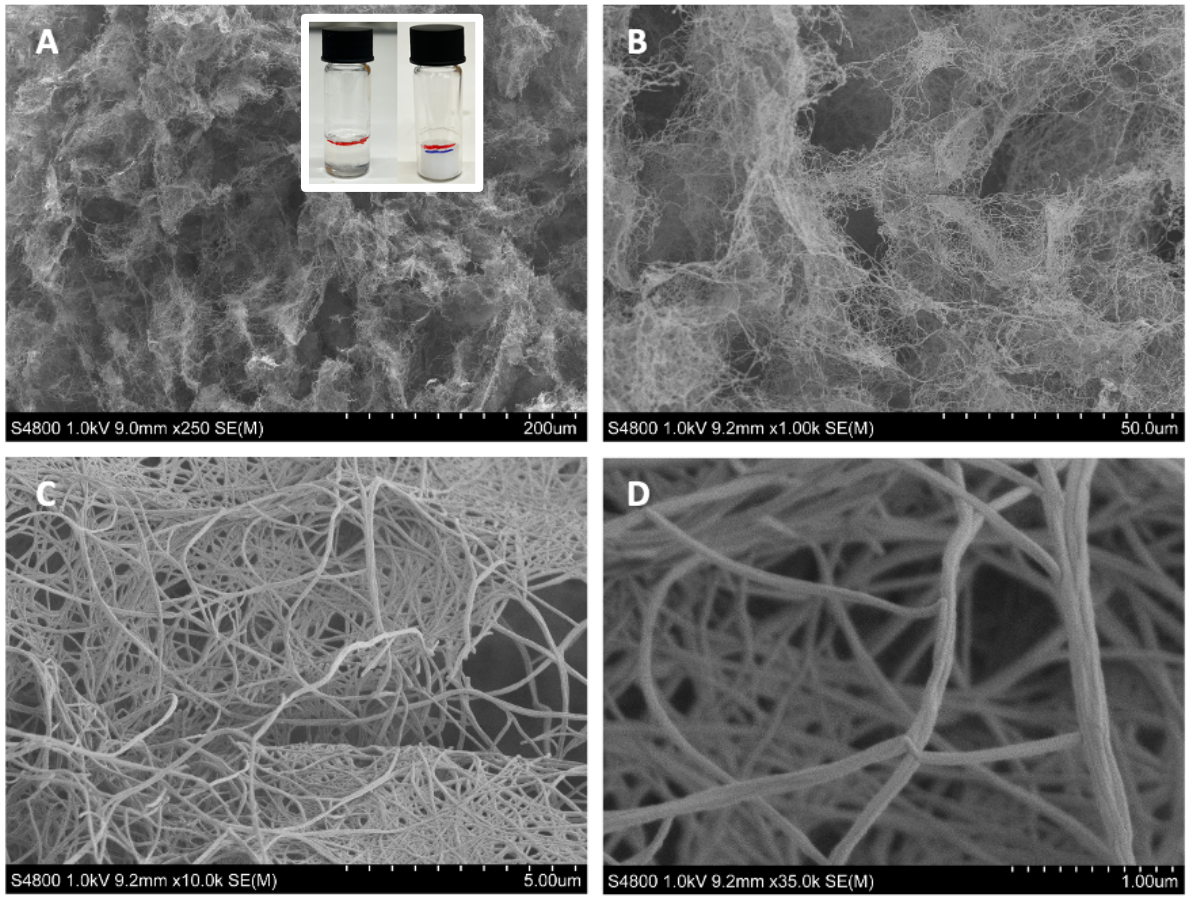

Figure S7. Aerogel of (*S*)-**SIA** from cyclohexane (1 mg / mL). (A, B) Top view of porous aerogel. Inset: difference in volume between gel and aerogel. (C) View of fibrous network of aerogel. (D) Individual fibres in the network.

Freeze-dried aerogel of (S)-SIA from cyclohexane below critical gel point

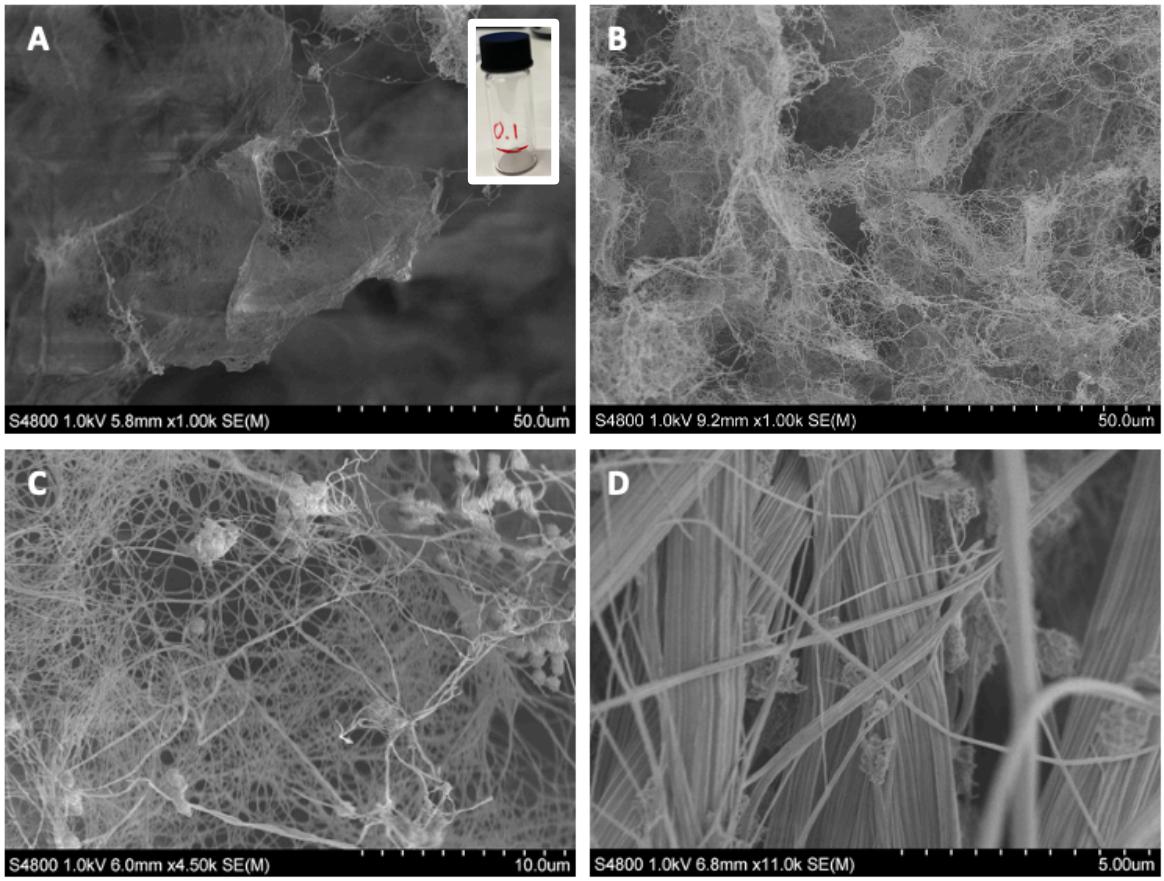

Figure S8. Aerogel of (*S*)-**SIA** from cyclohexane at 0.1 mg/mL (A, B) Top view of porous aerogel. Inset: difference in volume between original solvent volume and aerogel volume. (C) View of fibrous network of aerogel. (D) Individual fibres in the network.

UV-Vis and CD-spectroscopy

General: The UV-vis and CD measurements were carried out using a Chirascan CD spectrometer (Applied Photophysics) equipped with a Peltier temperature control system. The measurements were performed using a sample cell with 1 mm optical path length. The spectral region was recorded from 200 to 300 nm with a step size of 1 nm, a measurement time of 0.5 s per point and a bandwidth of 1 nm. The displayed spectra are averages of 5 individual scans for which the background signal has been subtracted and the amplitude corrected for the relative gelator concentrations as estimated by the absorbance spectra of the samples (collected in parallel). CD spectra were measured in heptane in order to minimize the background absorption in the wavelength range of interest. Samples with a concentration of 1 mg/ml were diluted 1:2 and 1:10 in heptane.

Time dependent UV-Vis measurement (Figure 5C): The kinetic experiments were performed by letting the temperature stabilize at 65 °C and then following the spectra evolution after changing the temperature to 25 °C.

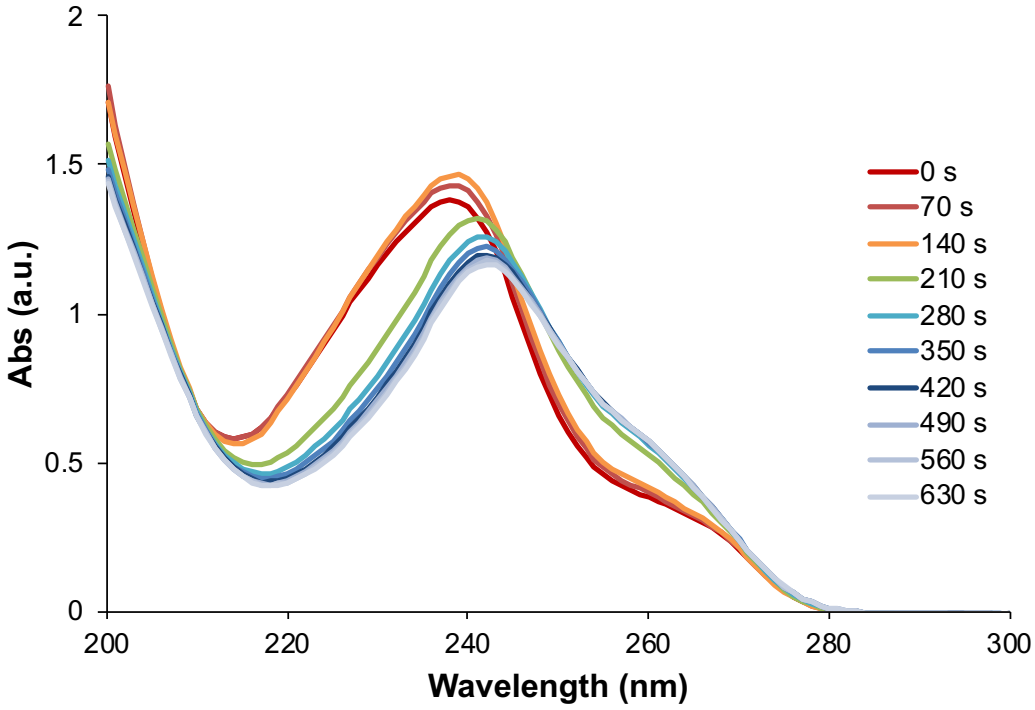

Figure S9. Time-dependent UV-vis spectrum of the transition from monomeric (***S***)-SIA (1.0 mg/mL) to the supramolecular polymer upon cooling from 65 °C to 25 °C.

Variable temperature UV-vis and CD-spectroscopy (Figure 5E)

The CD-spectra at different temperatures (15-65 °C) were measured via stepwise increase in temperature and the sample was equilibrated for at least 5 min at each temperature before measuring the CD spectrum.

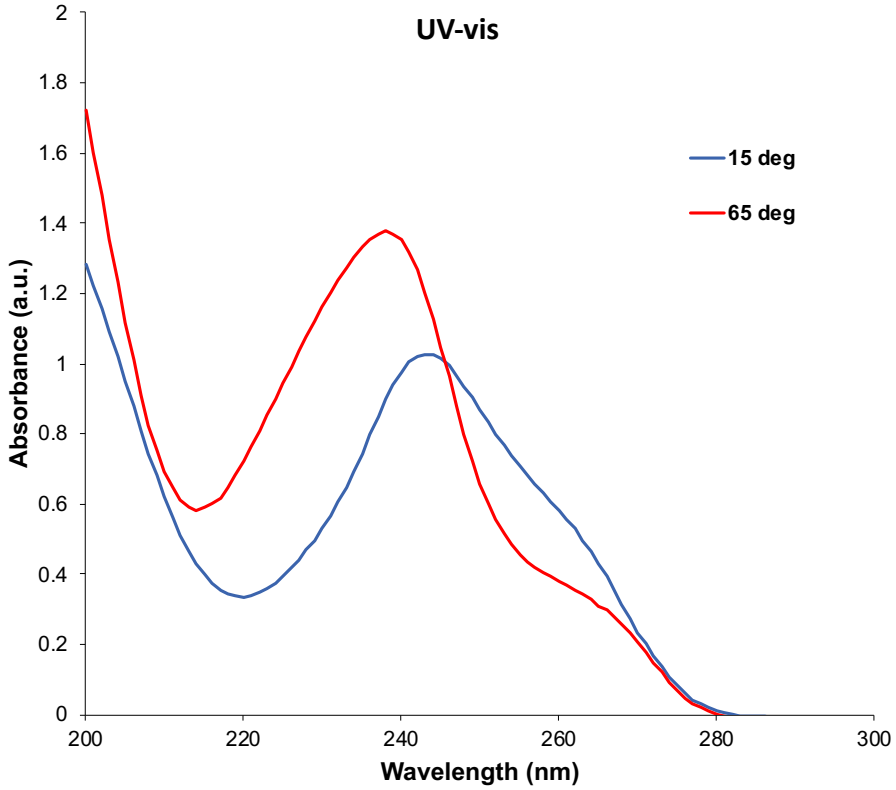

Figure S10. UV-Vis spectra of (***S***)-SIA (1.0 mg/mL) at 15 °C (supramolecular polymer) and 65 °C (monomers).

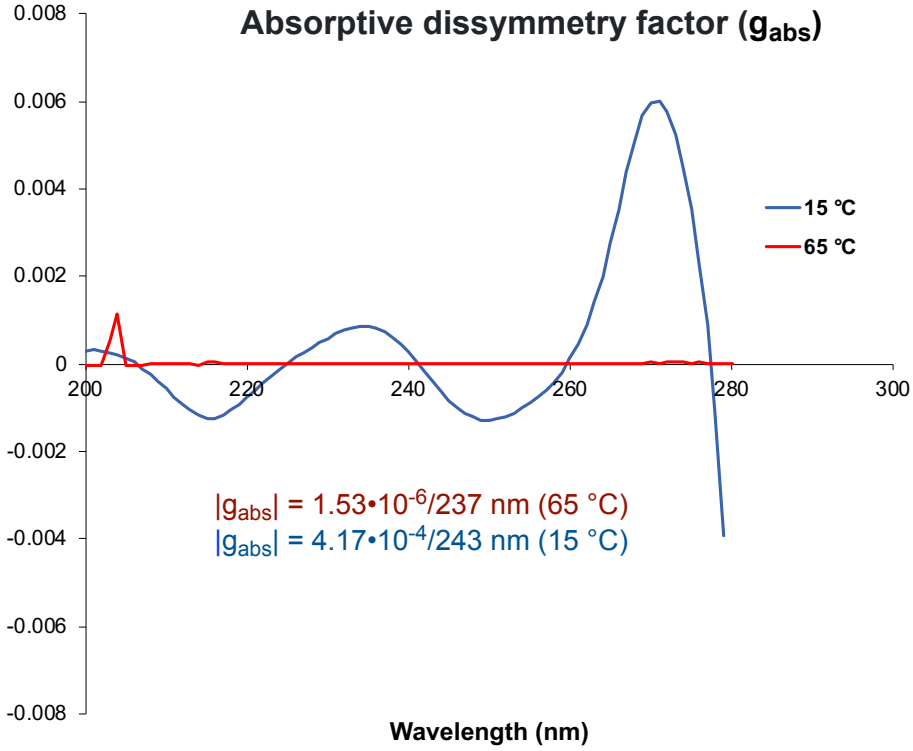

Figure S11. Quantification of the absorptive dissymmetry factor (g_{abs}) (ratio between molar CD to molar extinction coefficient) for (**S**)-SIA (1.0 mg/mL) at 15 °C (supramolecular polymer) and 65 °C (monomers). The g_{CD} spectra were computed as the ratio of molar CD to molar extinction coefficient for unpolarized light using g_{CD} = CD / (32980 · Abs). The absorptive dissymmetry factors (g_{abs}) were determined at the λ_{max} (abs).

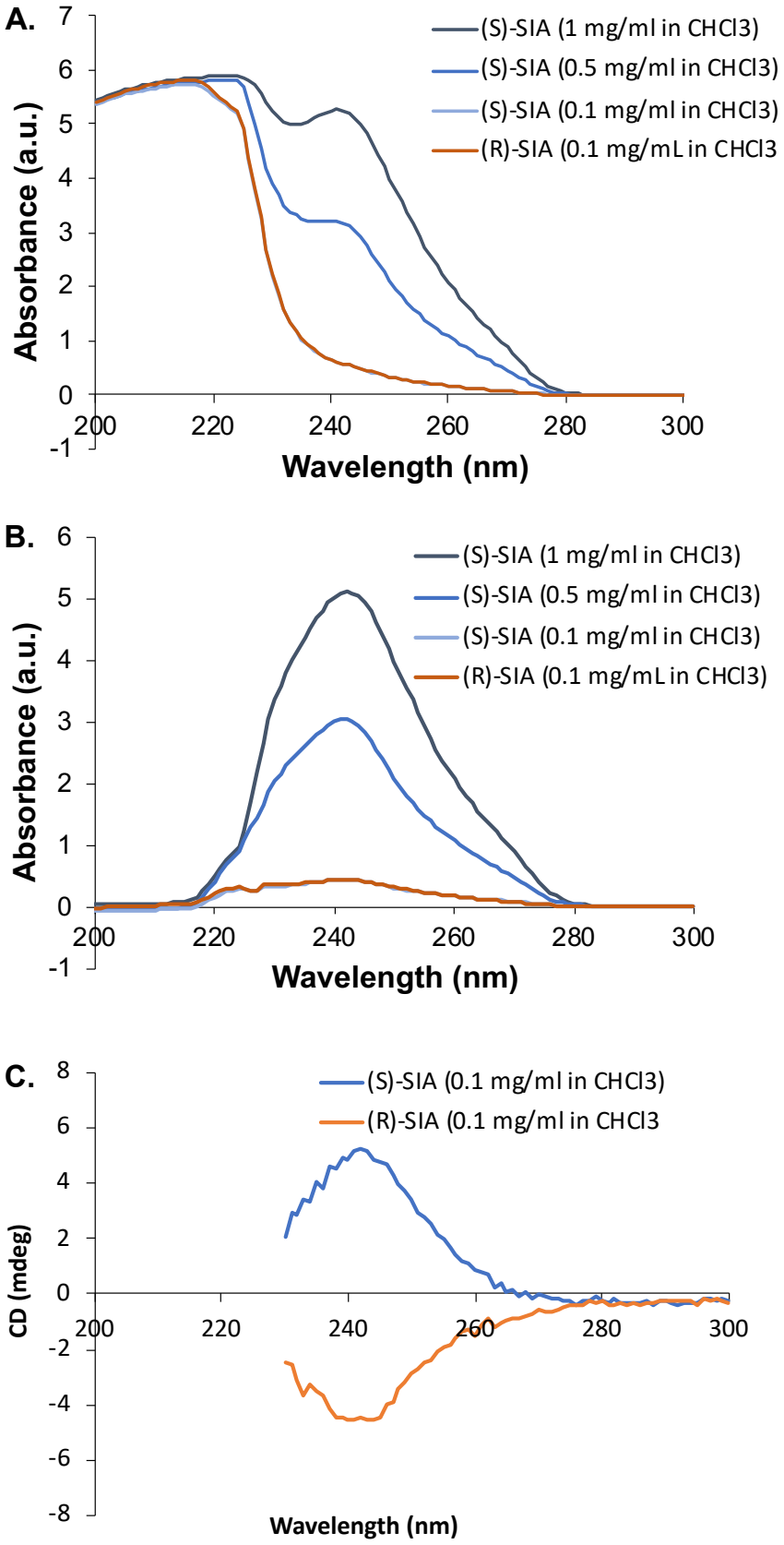

Figure S12. A) UV-vis spectra of (***S***)-SIA (0.1, 0.5 and 1.0 mg/mL) at 25 °C in $CHCl_3$. B) UV-vis spectra of (***S***)-SIA (0.1, 0.5 and 1.0 mg/mL) at 25 °C in $CHCl_3$ with subtracted chloroform background. C) CD-spectrum at of (***S***)-SIA (0.1 mg/mL, below CGC) in $CHCl_3$.

NMR-spectroscopy

Temperature-dependent ^{19}F NMR spectra:
The ^{19}F NMR (376.5 MHz) spectra were recorded on a Bruker Avance-III HD spectrometer using a 5 mm "smart" probe. The NMR sample was prepared by dissolving (*S*)-**SIA** (0.5 mg/ml) in normal heptane (non-deuterated). The experiments were run in a 5 mm NMR tube without deuterium lock. 64 FIDs were collected for each spectrum using a 3 s relaxation delay between the scans. The temperature dependence of monomer concentration was studied in the range of 60-15 °C by decreasing the temperature in 5 °C increments. The probe temperature was measured by a calibrated Pt-100 resistance thermometer and adjusted using the standard Bruker temperature control unit. The sample was allowed to equilibrate at each temperature for 5 min before recording the spectra. Hexafluorobenzene was used as an internal standard to calibrate and compare the change in signal intensities of (*S*)-**SIA** between the spectra.

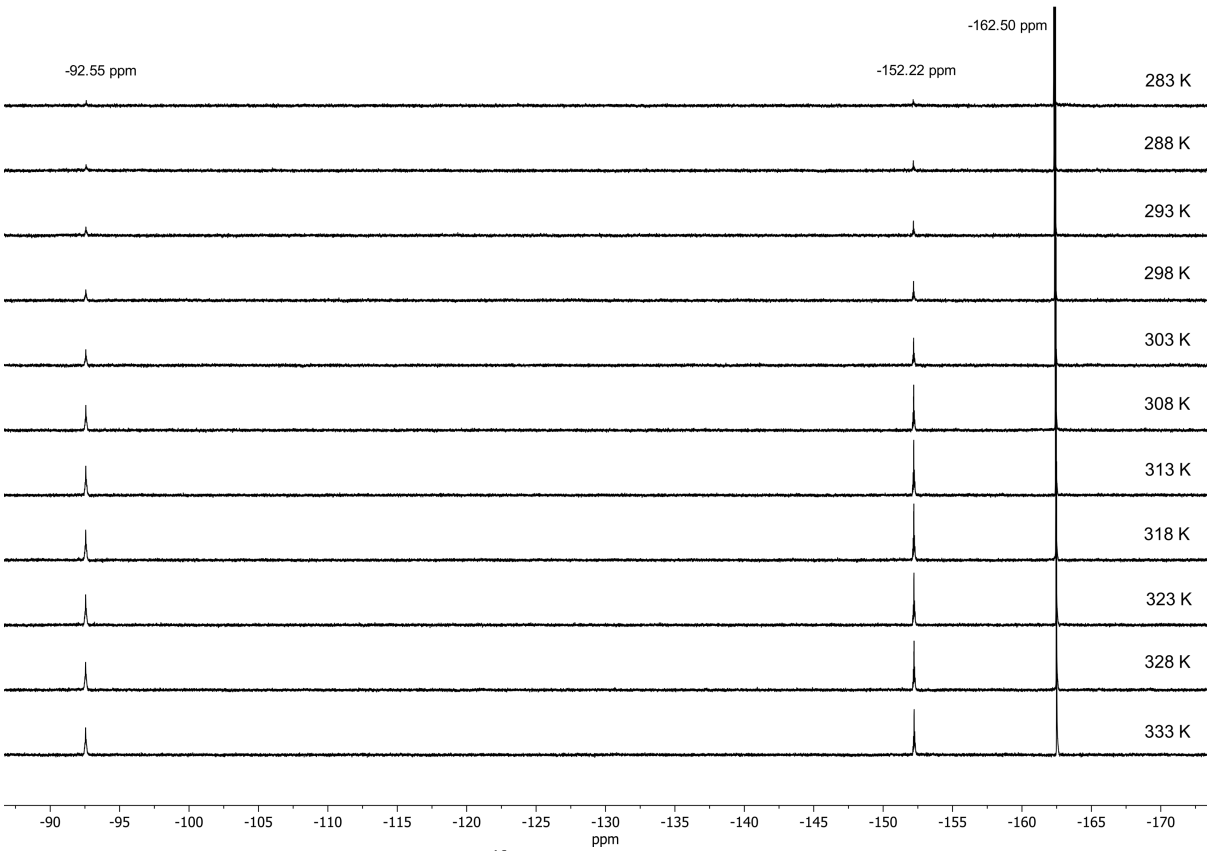

Figure S13. Stacked, temperature-dependent ^{19}F spectra of (*S*)-**SIA** in heptane at 283 K to 333 K using hexafluorobenzene as internal standard.

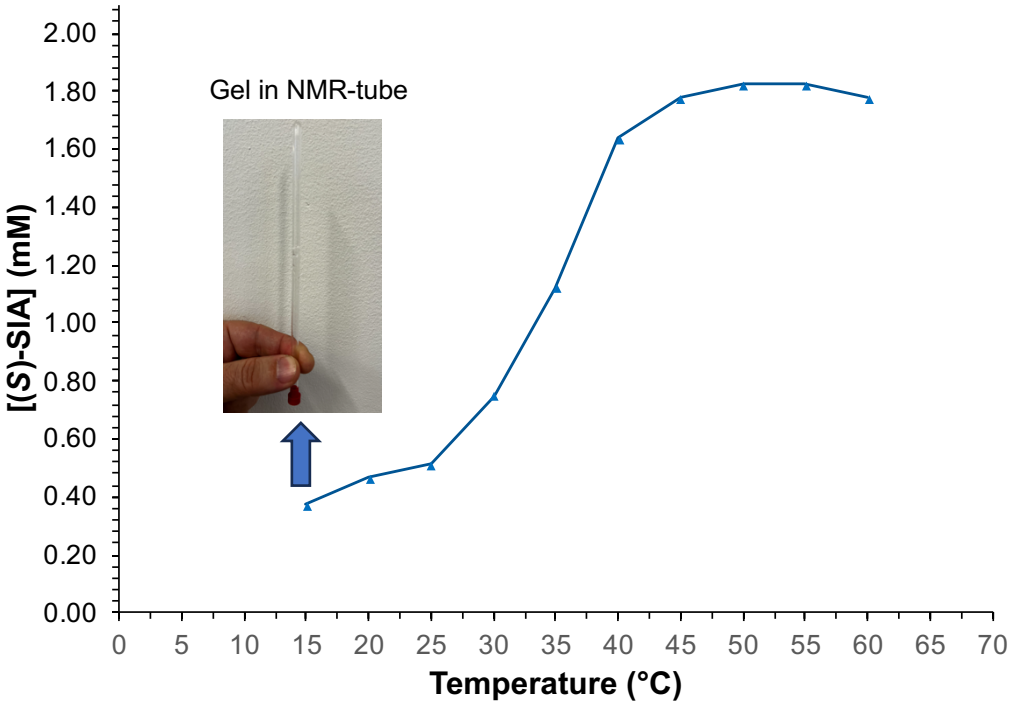

Figure S14. Temperature-dependence of supramolecular polymerization from ^{19}F NMR-spectra upon incremental cooling of (*S*)-**SIA** dissolved in heptane at 60 °C to organogel at 15 °C. Inset: formation of organogel at 15 °C after performed experiment.

Concentration-dependent ^{19}F NMR spectra:

The ^{19}F NMR (376.5 MHz) spectra were recorded on a Bruker Avance-III HD spectrometer using a 5 mm "smart" probe. The NMR sample was prepared by dissolving (*S*)-**SIA** (0.31 mg/ml) in normal heptane (non-deuterated, 0.5 mL) and hexafluorobenzene was used as an internal standard to calibrate and compare the change in signal intensities of (*S*)-**SIA** between the spectra. The experiments were run in a 5 mm NMR tube without deuterium lock collecting 64 FIDs for each spectrum using a 3 s relaxation delay between the scans. The concentration dependence of monomer in solution was studied at 293 K by sequential dilution of the sample with heptane and additional spectra was recorded.

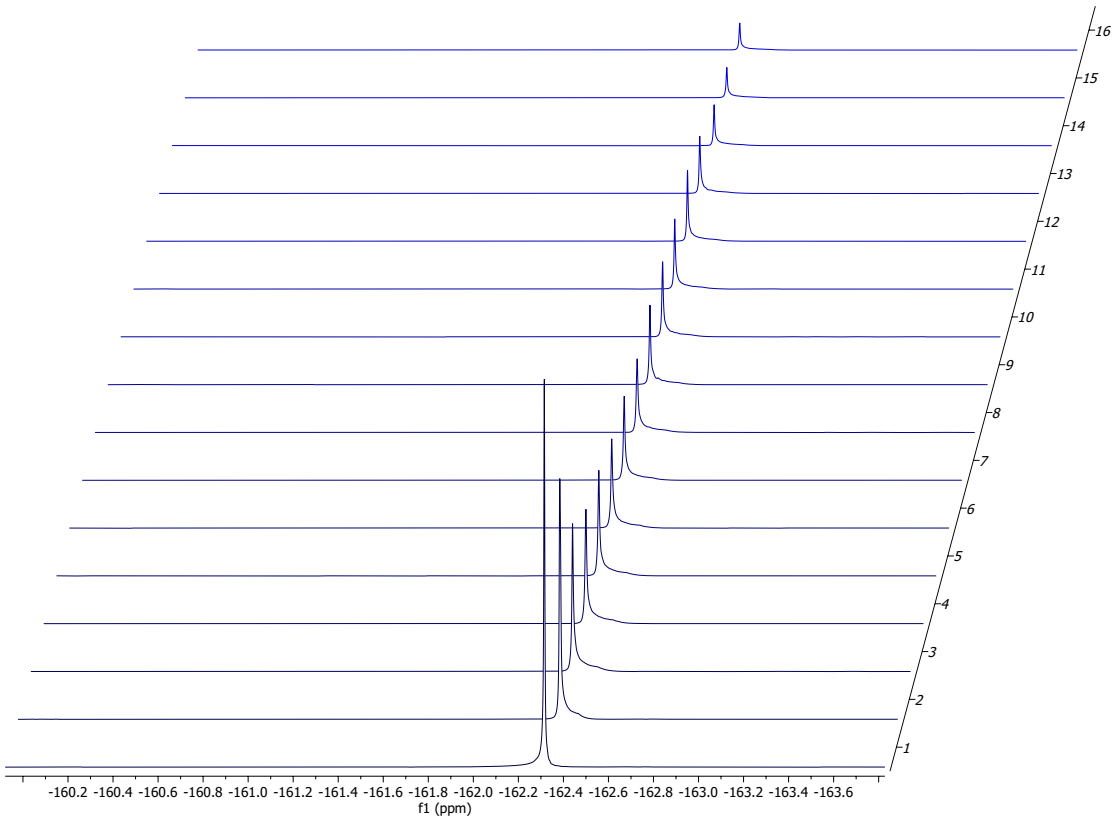

Figure S15. Stacked concentration dependent ^{19}F spectra showing the influence of dilution of the internal standard signal (hexafluorobenzene) in heptane at 293 K.

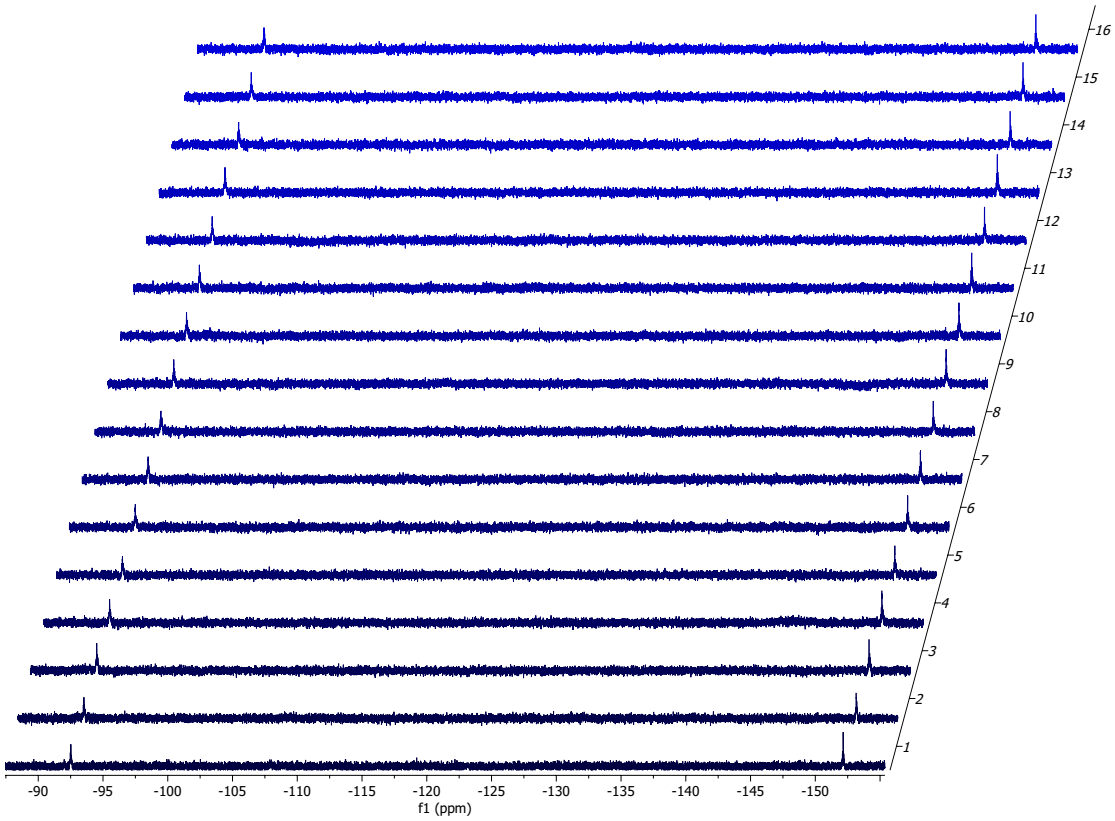

Figure S16. Stacked concentration dependent ^{19}F spectra showing the signals of the monomer ((*S*)-**SIA**) in heptane at 293 K.

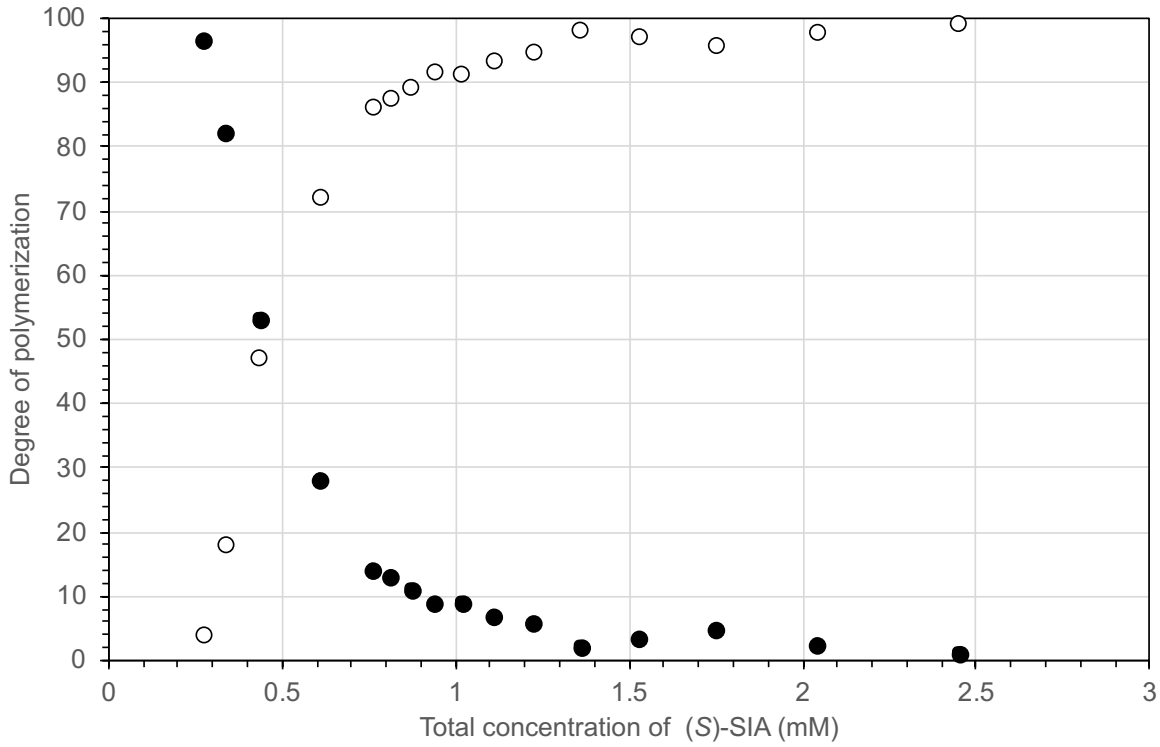

Figure S17. Degree of polymerization (O) as calculated from ^{19}F spectra of the monomer (•) of (*S*)-**SIA** in heptane at 293 K.

IR spectroscopy

Three IR spectra from the organogelator for solution in chloroform (blue line: 4.8 mg/mL, below CGC), organogel from chloroform (orange line: 28 mg/mL) and from xerogel (red line).

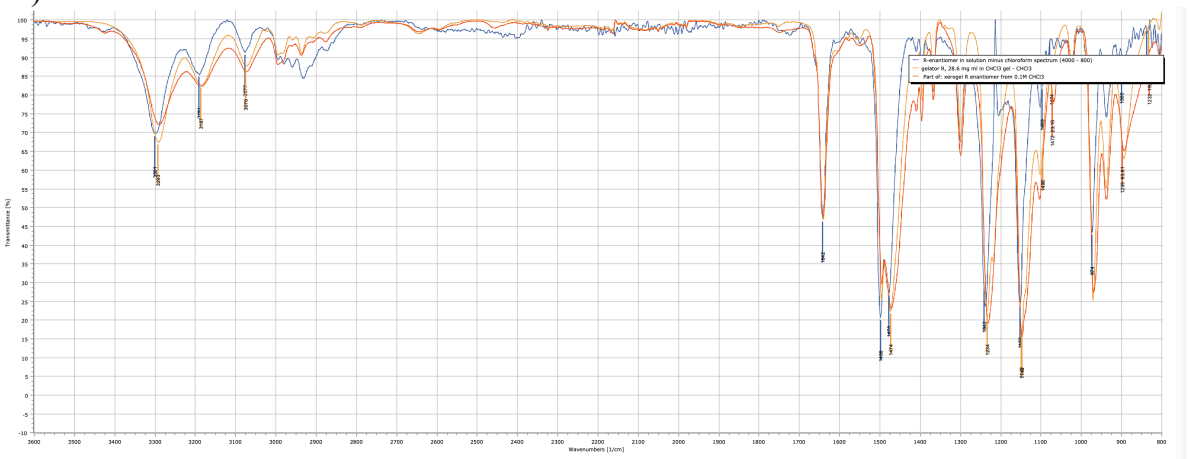

Figure S18. IR-spectra of solution of (*R*)-**SIA** (blue line: 4.8 g/mL in chloroform, below CGC), Organgel of (*R*)-**SIA** (orange line: 28 mg/mL in chloroform) and xerogel (*R*)-**SIA (**red line**).**

Computational details

Force field parametrization

The ground state geometry optimization of perfluorinated sulfonimidamides (SIA) structure was carried out in Gaussian[1] (version 16.C.01) by employing B3LYP[2–4] density functional theory (DFT) and aug-cc-pVDZ[5] basis set. Next, for the optimized geometry of (*R*)-SIA, the initial force field parameters were obtained from the General Amber Force Field[6,7] (GAFF) database. The Restrained Electrostatic Potential[8] (RESP) charges were calculated at HF/6-31G* on the B3LYP optimized geometry in the gas phase.

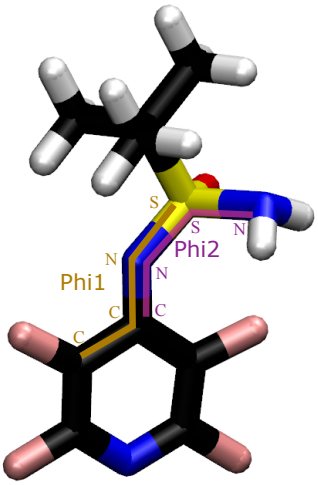

Figure S19. Molecular structure of (*R*)-SIA represented in licorice with marked important rotatable dihedrals CCNS (Phi1) and CNSN (Phi2).

The initial parameters were further improved in order to correctly described a dihedral potential of rotatable bonds and optophysical properties. All the reference bond distance and bond angle parameters in the initial force field were replaced with bond distances and bond angles of B3LYP optimized geometry. The two important dihedrals in the (*R*)-SIA structure (marked in Figure S19) were fitted to DFT potentials. The DFT potentials were computed at B3LYP/aug-cc-pvdz. The results of Molecular Mechanics (MM) potentials after fitting the dihedrals and their comparison with DFT potentials are shown in Figure S20. For both the dihedrals Phi1 and Phi2, MM potential reasonably emulates the DFT potentials.

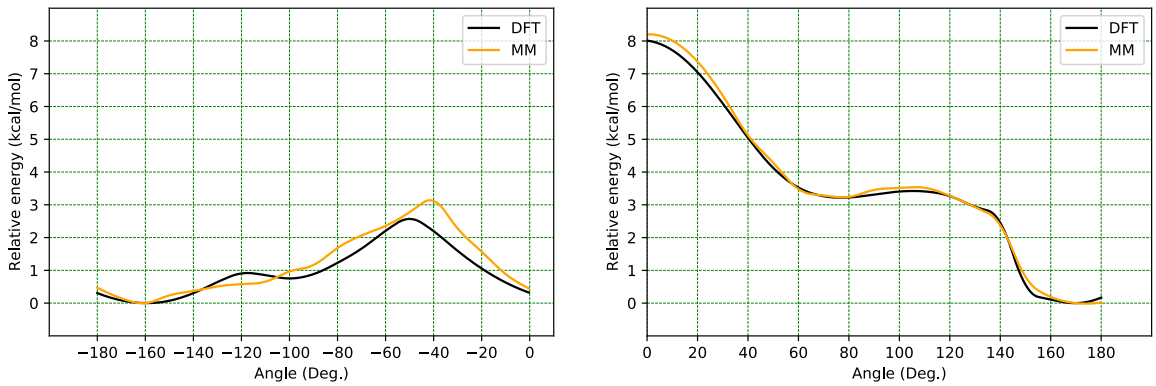

Figure S20. Dihedral potentials comparison between DFT (B3LYP) and MM (reparametrized forcefield) method for Phi1 and Phi2 (marked in Figure S19).

Table S1. Comparison of DFT vs. MM ground state energies and transition wavelengths for (*R*)-SIA conformers.

		Relative energy (kcal/mol)			Transition wavelength in nm [eV]		
	Phi1_value	DFT	MM	Error	DFT	MM	Error
Conf1	-100	0.72	0.48	0.2	239 [5.19]	246 [5.05]	7 [0.14]
Conf2	-160	0.0	0.1	0.1	237 [5.22]	243 [5.11]	6 [0.11]
Conf3	23	0.0	0.0	0.0	237 [5.22]	244 [5.08]	7 [0.14]

For the validation of the parametrized force field, three conformers lying on the minima of Phi1 dihedral potential were selected. The relative energies of MM optimized and B3LYP optimized geometries were compared for these three conformers (Table S1). The maximum error of 0.2 kcal/mol for the local minima was within the expected range of error in B3LYP. On each optimized geometries obtained from B3LYP and MM methods, single-point absorption spectra were calculated with CAM-B3LYP[9] functional and aug-cc-pVDZ basis set in the Dalton program[10] (version 2018.alpha). The maximum error in transition wavelength estimation is 7 nm (or 0.14 eV).

Molecular modelling

Four molecules of (*R*)-SIA are assembled into a monomer unit by forming a hydrogen bonding network. The choice of hydrogen bond type was based on consideration of the functional groups in the (*R*)-SIA molecule and the associated test calculations. Within the monomer unit, an intramolecular hydrogen bonding network was constructed between the H atom of NH2 and the N atom of the pyridine group from two adjacent (*R*)-SIA molecules (Figure S21).

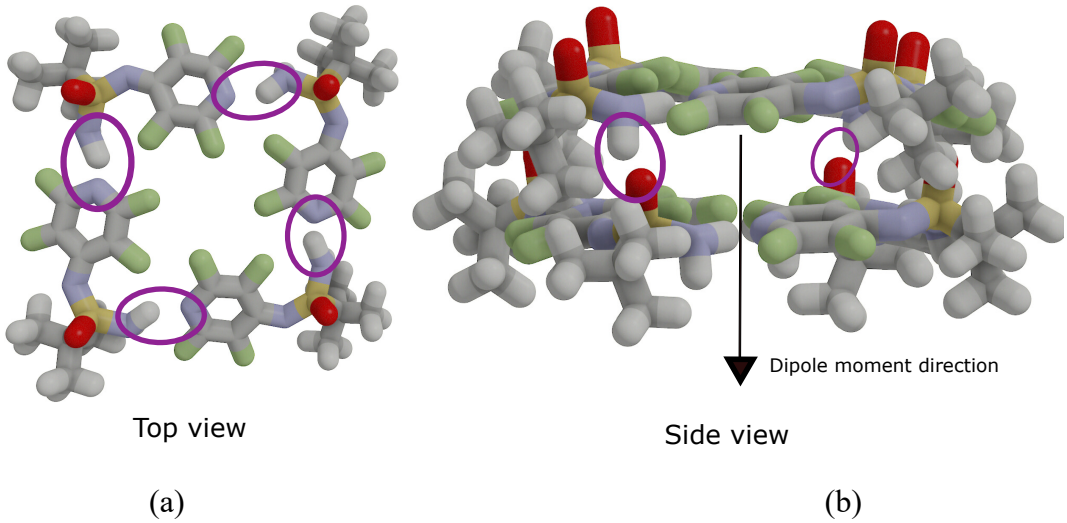

Figure S21. The highlighted purple regions show the hydrogen bonding interactions. (a) Top view of monomer unit showing hydrogen bonding network. (b) Side view of dimer unit with dipole moment direction.

Next, a vertical stack of monomer units was built using the MM geometry optimized structure of a model monomer with a 4 Å distance and a -24 degree twist between two adjacent monomer units on a stack. An M-type helical fibre was first constructed by stacking 16 monomer units vertically based on experimental information about the helical structure. As a result of this M-type conformation, a vertical hydrogen bonding network is formed between the top-layer H atom of the NH_2-group in (*R*)-SIA and the bottom-layer O atom in (*R*)-SIA.

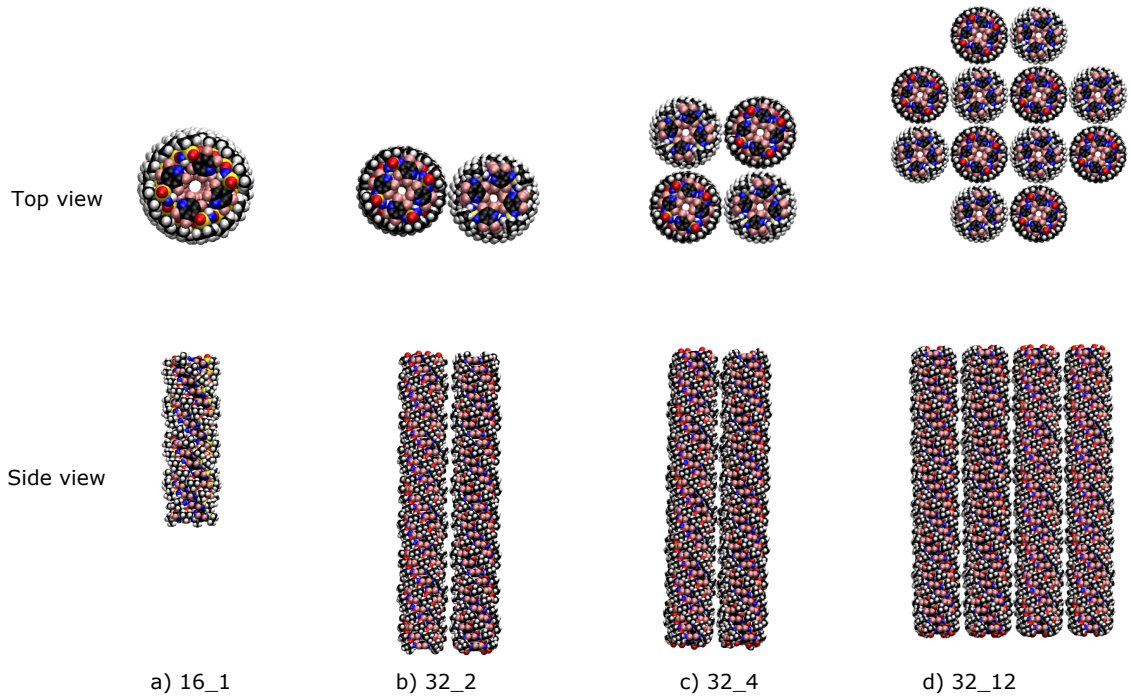

Figure S22. Molecular configurations built from monomer unit made of four (*R*)-SIA molecules. The first number shows number of monomer units and number following underscore shows number of helical stacks in a system. a) 16 monomer units, forming one helical stack. b) 32 monomer units and two helical stacks. c) 32 monomer units and four helical stacks. d) 32 monomer units and twelve helical stacks.

The dipole moment of the monomer unit is non-zero in the z-direction. Therefore, the dipole moment adds up upon the vertical addition of the monomer unit in the direction of a helical axis (see Figure S21b). In order to lower the system dipole moment, another helical stack was constructed but placed in the opposite direction (see Figure S22b). Similarly, multiple possible configurations of helical stacks were built to perform MD simulation (Figure S22).

Molecular Dynamic Simulations

All classical MD simulations were performed using GROMACS[11–14] (version 19.3) with the reparametrized GAFF for the (*R*)-SIA molecules and GAFF for heptane solvent molecules. All three directions of the simulation box were subjected to periodic boundary conditions. A 1.2 nm long-range cutoff was used to simulate electrostatic interactions using the Particle Mesh Ewald[15] (PME) approach. The cutoff distance for Lennard-Jones interactions was also equal to 1.2 nm. The MD simulation time step was 2 fs with a pair-list update period of 10 steps.

Molecular Dynamic Simulation of helical stack 16_1 (Figure. 22a):

Starting from the helical fibre with 16 vertically stacked tetramer units as described above, it was first energy minimized with the GROMACS's steepest decent algorithm. Next, it was solvated with heptane molecules in a simulation box of size 10nm x 10nm x 10nm, and again the energy was minimized. To correct the system's density and the solvent molecules' orientation around the helical stack, NPT equilibration was performed for 100 ps while applying position restraints to the helical stack. The position restraint was then removed, and the system was simulated for 100 ps in NPT at 1K. This was done to avoid any possible significant distortion in the helical structure upon removing position restraints. The system was then gradually heated to 300K in 90ns by employing a simulated annealing procedure. The helical stack was observed to start deforming from approximately 170K onwards.

Molecular Dynamic Simulation of helical stack 32_2, 32_4, and 32_12 (Figure S22b, S22c, and S22d):

For these systems, the process followed was the same as outlined for the helical stack system 16_1, except that the heating from simulated annealing was stopped after it reached the temperature of 100K. Then for each system, MD simulations were run at 100K for 26 ns. For the helical system 32_12, it was further heated to 150 K, followed by an extra equilibrium MD simulation at the temperature of 150K for 30ns.

Results from MD simulation

The experimental information was used to model the final helical fibres 32_12 system. It was built progressively, as described in the "Molecular Modelling" section. Below are the results from the 30 ns MD simulation of the final 32_12 system. All the distance analysis were performed using Kernel Density Estimation (KDE) plot from the seaborn python library[16].

To evaluate the strength of hydrogen bonding interactions, the distance d1 and the distance d2 were computed (see Figures S23a and S23b). The distance d_1 is between atom type N1 and atom type H1 or H2 on two adjacent (*R*)-SIA molecules. In each monomer unit, a set of 8 pairs (4 N1-H1 and 4 N1-H2) distances were computed. The distance d_2 is between atom type O1 and atom type H1 or H2 on another (*R*)-SIA molecule placed on top or bottom in a vertical stack of monomers. Hence, 16 pair (O1-H1 or O1-H2) distances exist between three monomers stacked vertically. For the non-terminal monomer unit, the set of three monomers instead of two was chosen for the calculation because the oxygen atom (type O1) points upward in some vertical stacks, and in others, it points downward. Next, the distances d_1 and d_2 were aggregated over each monomer set within the snapshot and over the MD trajectory of 30 ns.

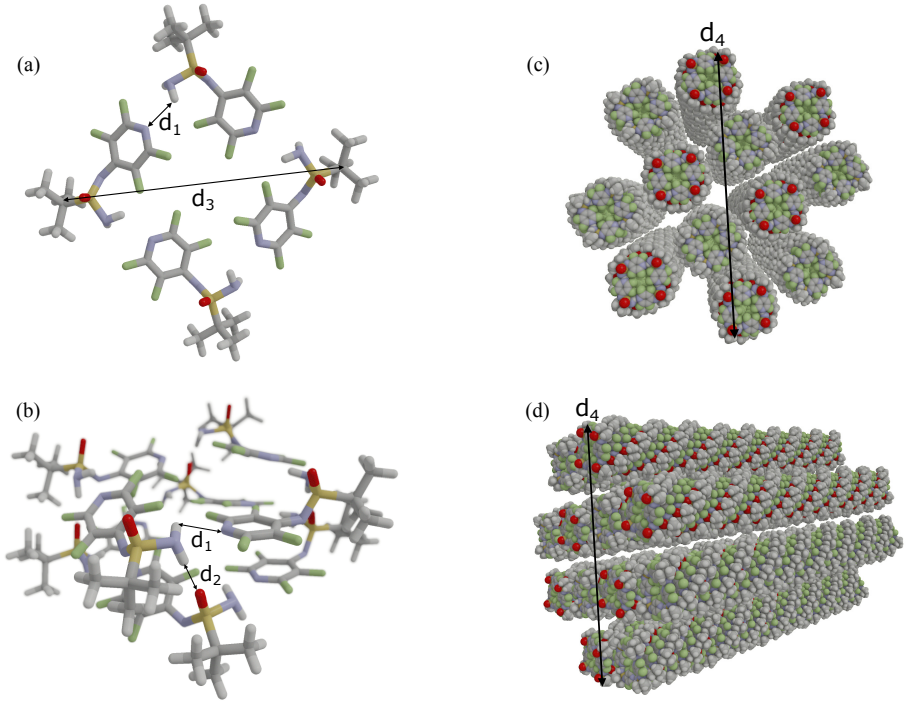

Figure S23. Labelled distances to evaluate the strength of hydrogen bonding (from d_1 and d_2), length of monomer unit (from d_3) and cluster of helical stacks (from d_4). (a) Top view of monomer unit. (b) Perspective view of dimer unit. (c) Top view of cluster of helical stacks. (d) Perspective view of cluster of helical stacks.

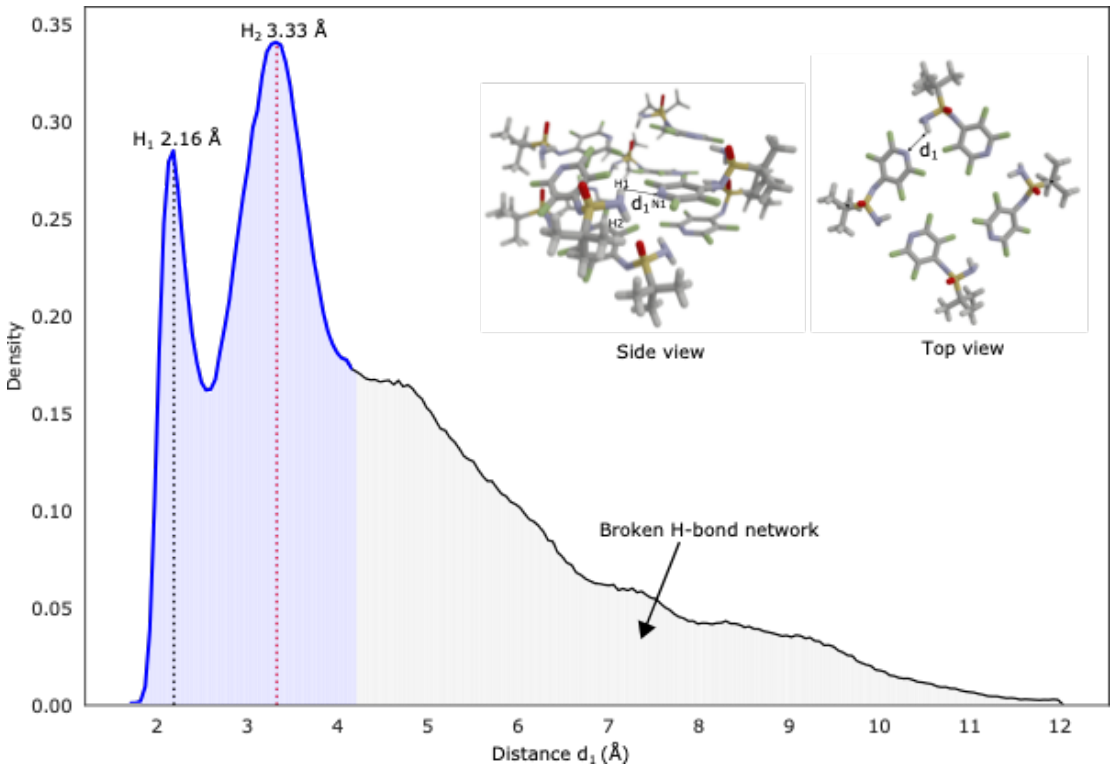

Figure S24. KDE plot of distance d1 between atom type N1 and atom type H1 or H2 on another adjacent (*R*)-SIA molecule. The shaded grey region shows the broken hydrogen bonding network of type (N–H--N).

From the KDE plot of distance d_1, the two peaks corresponding to two hydrogens of NH_2 groups (Figure S24). One of them participate in intermolecular hydrogen bonding interaction with nitrogen atom from pyridine group with the distance of 2.16 Å. The less populated shaded grey part shows the broken hydrogen bonding integration with the pyridine's N atom and instead it forms hydrogen bonding with F atom on pyridine group. The KDE plot of distance d_2 also shows two peaks associated with two hydrogens of NH_2 groups (Figure 25).
Since d_2 contains all the possible distances between atom type O and atom type H1 and H2 of NH_2-group between two consecutive monomer units, the d_2 range extends above 5 Å. The first peak represents intermolecular hydrogen bonding interaction with distance 1.92 Å between oxygen and hydrogen atoms. The d_2 hydrogen bonding interaction is stronger than the d_1.

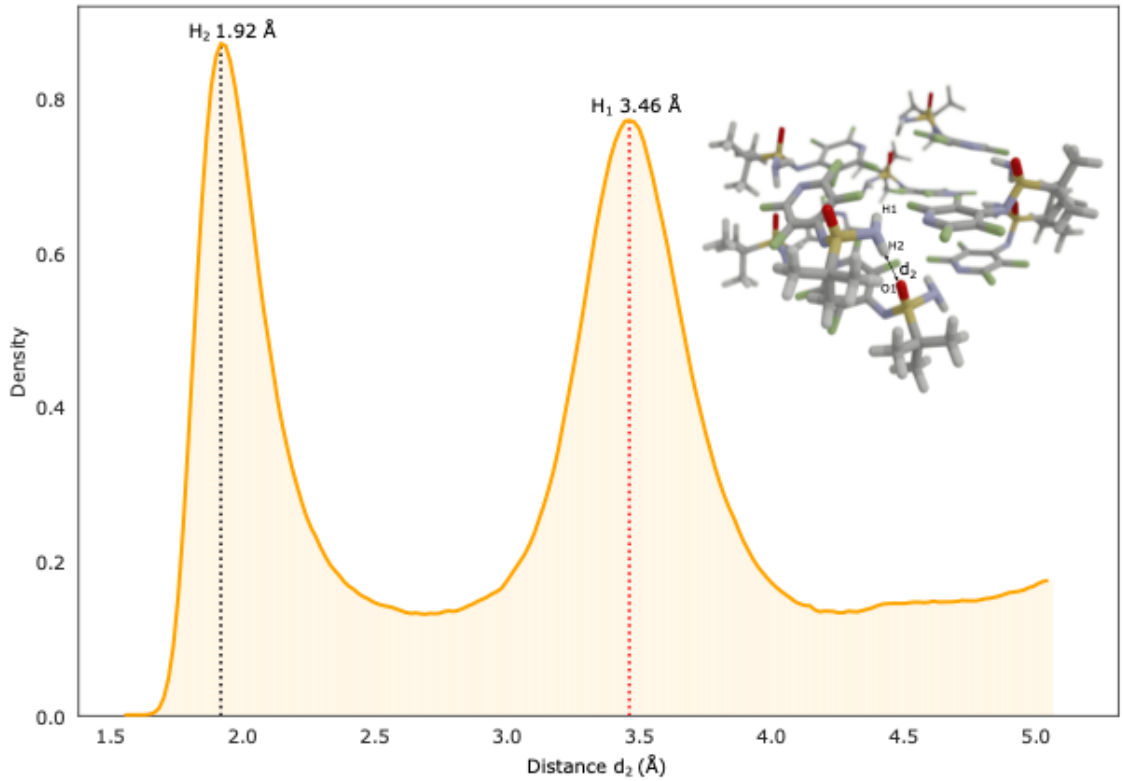

Figure S25. KDE plot of distance d_2 between the atom type O1 and atom type H1 or H2 on another (*R*)-SIA molecule placed on top or bottom in a vertical stack of monomers.

The dimension of the monomer unit or cluster of helical stack obtained from the atomistic model facilitates understanding of the macroscopic picture obtained from scanning electron microscopy (SEM).

The distance d_3 is between two C6 atom types diagonally placed on (*R*)-SIA molecules in the monomer unit (see Figure S26). The two diagonal pair (C6-C6) distances were computed in each monomer unit and were aggregated over all 384 monomer units (32 x 12) and the simulation trajectory. The distance d_4 is between two C6 atom types from (*R*)-SIA molecules on the same horizontal level in the cluster of 12 helical stacks (see Figures S23c and S23d). For each horizontal layer of the cluster, the diagonally placed two monomers contain 16 pairs of C6-C6 distance. Out of which only the maximum value is selected as it corresponds to the distance d_4 marked in Figure 26. Next, all the d_4 distances were aggregated over all the 32 horizontal layers of the cluster and the simulation trajectory.

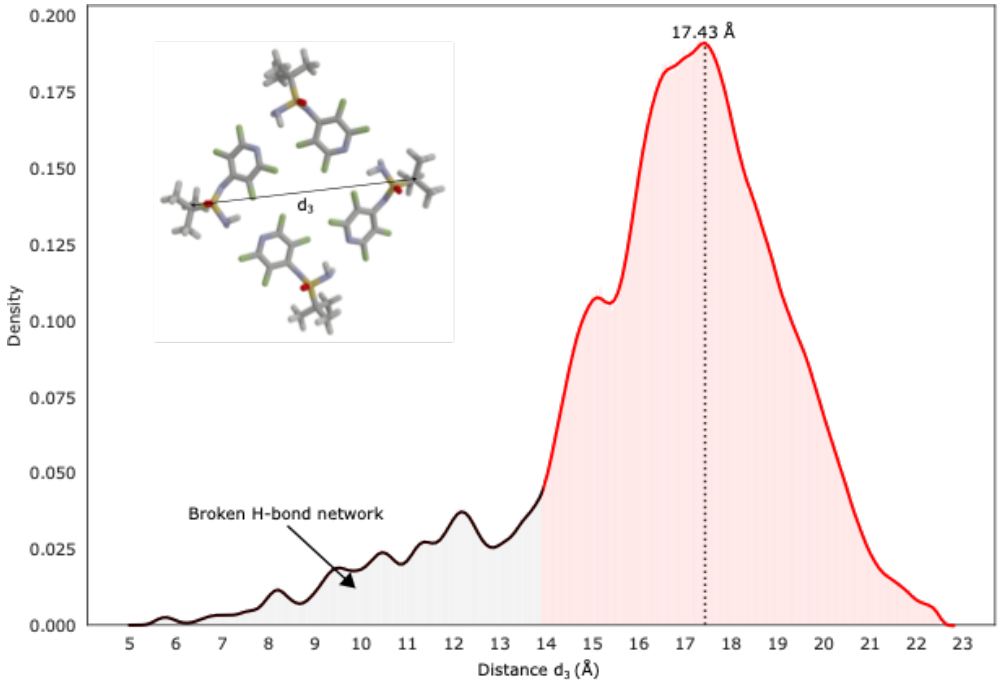

Figure S26. The KDE of distance d_3 between the two C6 atom types placed on two diagonal (R)-SIA molecules in a monomer. The shaded grey region highlights the broken hydrogen bonding network of type N–H--N in a few monomer units as seen in Figure S24.

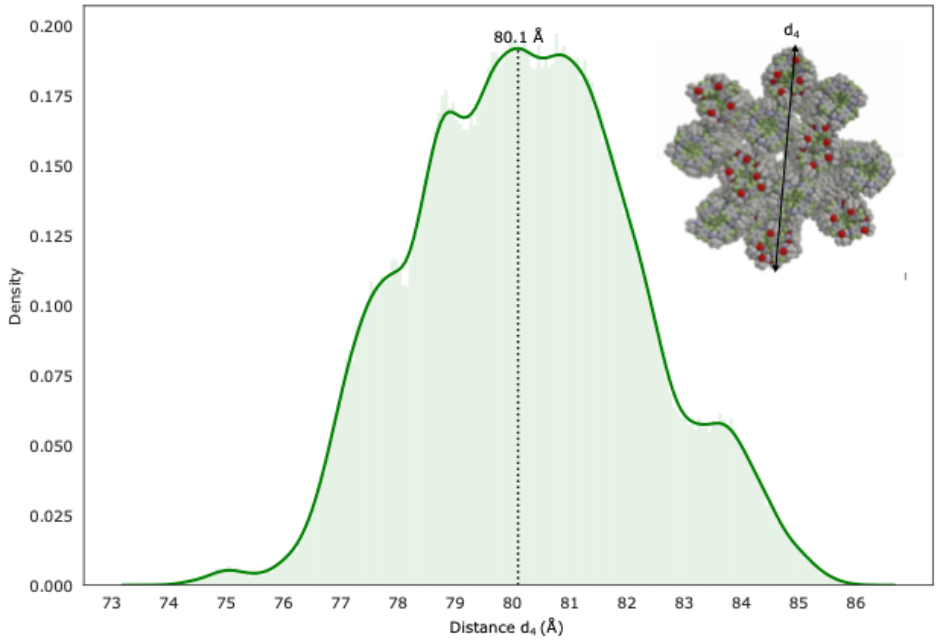

Figure S27. The KDE plot of distance d_4 between two C6 atom types from diagonally placed two monomers on the same horizontal level in the cluster of 12 helical stacks

As seen in the KDE plot of d_3 (Figure S26), the diagonal size of the monomer unit peaks around 17.4 Å. The shaded grey region again highlights the broken hydrogen bonding network as seen in KDE of d_1. From the d4 KDE plot (Figure S27), the cluster of 12 helical stacks has a cross-section peaking at around 80.1 Å. The narrow range of the d_4 KDE plot depicts stability of the cluster at 150 K.

Theoretical calculations of UV and CD spectra

The computational analysis was conducted on the UV and CD spectra of a specific molecular system. This system consisted of a two-layer unit containing 8 (*R*)-SIA molecules, extracted from the core of a larger 16-layer helical stack. To ensure accuracy, the geometry of the entire helical stack was optimized, both in the presence and absence of heptane solvation, using Molecular Mechanics (MM). The focus was on the spectral calculations of the extracted two-layer unit.

The analysis employed two computational chemistry programs: Gaussian and VeloxChem[17]. The UV absorption and CD spectra of the two-layer unit were compared using different methods (CAM-B3LYP/def2-svpp vs B3LYP/def2-svpd) and in different environments (heptane vs. vacuum). In addition, the CD spectra calculated with TD-DFT were also compared with spectra calculated using the CPP approach. Moreover, these results were juxtaposed with single molecule spectra in vacuum calculated using the CAM-B3LYP/def2-svpp method. The calculations for the CAM-B3LYP/def2-svpp method were performed using Gaussian, while those for the B3LYP/def2-svpd method were carried out in the VeloxChem program.

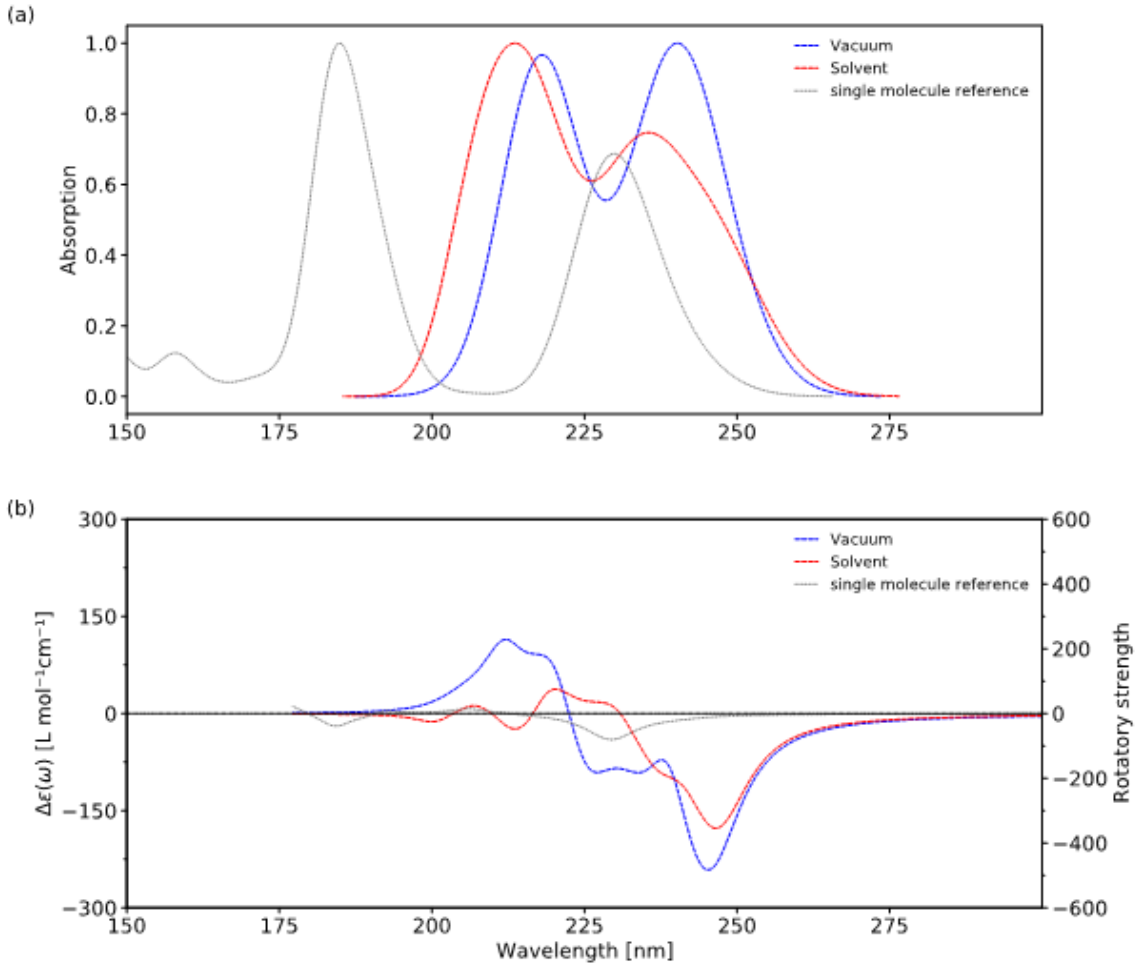

Figure S28. Comparative spectral analysis of dimer structures in different environments. Panel (a) depicts the UV absorption spectra, while panel (b) shows the circular dichroism spectra. Both panels compare the spectra of dimer structures optmized in vacuum and in heptane, with an additional reference to the spectra of a single molecule in vacuum. All the calculations were conducted with the CAM-B3LYP/def2-svpp method, focusing on 40 electronic states using the TD-DFT approach.

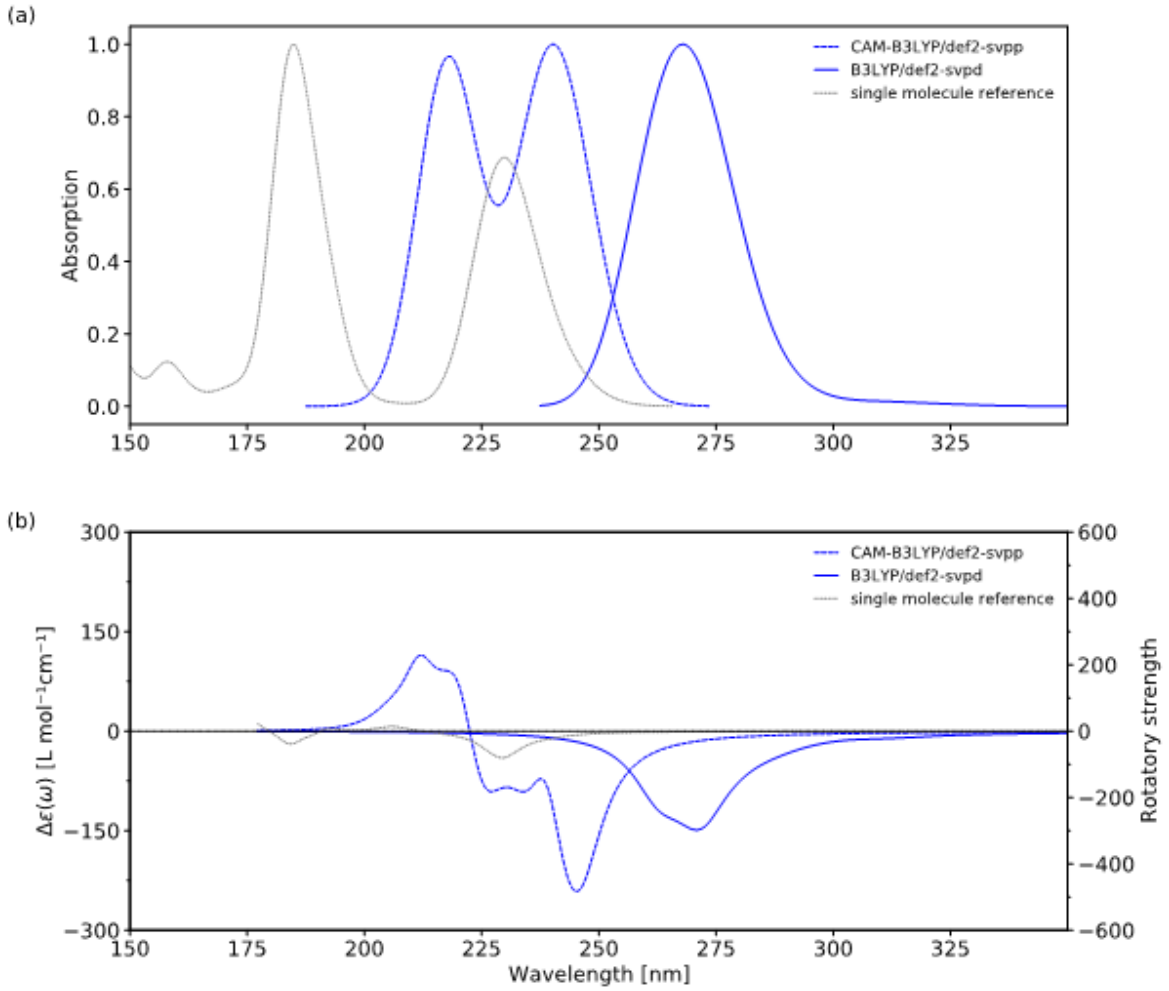

Figure S29. Comparative spectral analysis of dimer structures using different computational methods. Panel (a) depicts the UV absorption spectra, while panel (b) shows the circular dichroism spectra. Both panels illustrate the comparison between spectra calculated using two distinct methods: CAM-B3LYP/def2-svpp and B3LYP/def2-svpd. Additionally, the spectra of a single molecule calculated using the CAM-B3LYP/def2-svpp method are included for reference. All spectra are computed in vacuum, focusing on 40 electronic states via the TD-DFT approach.

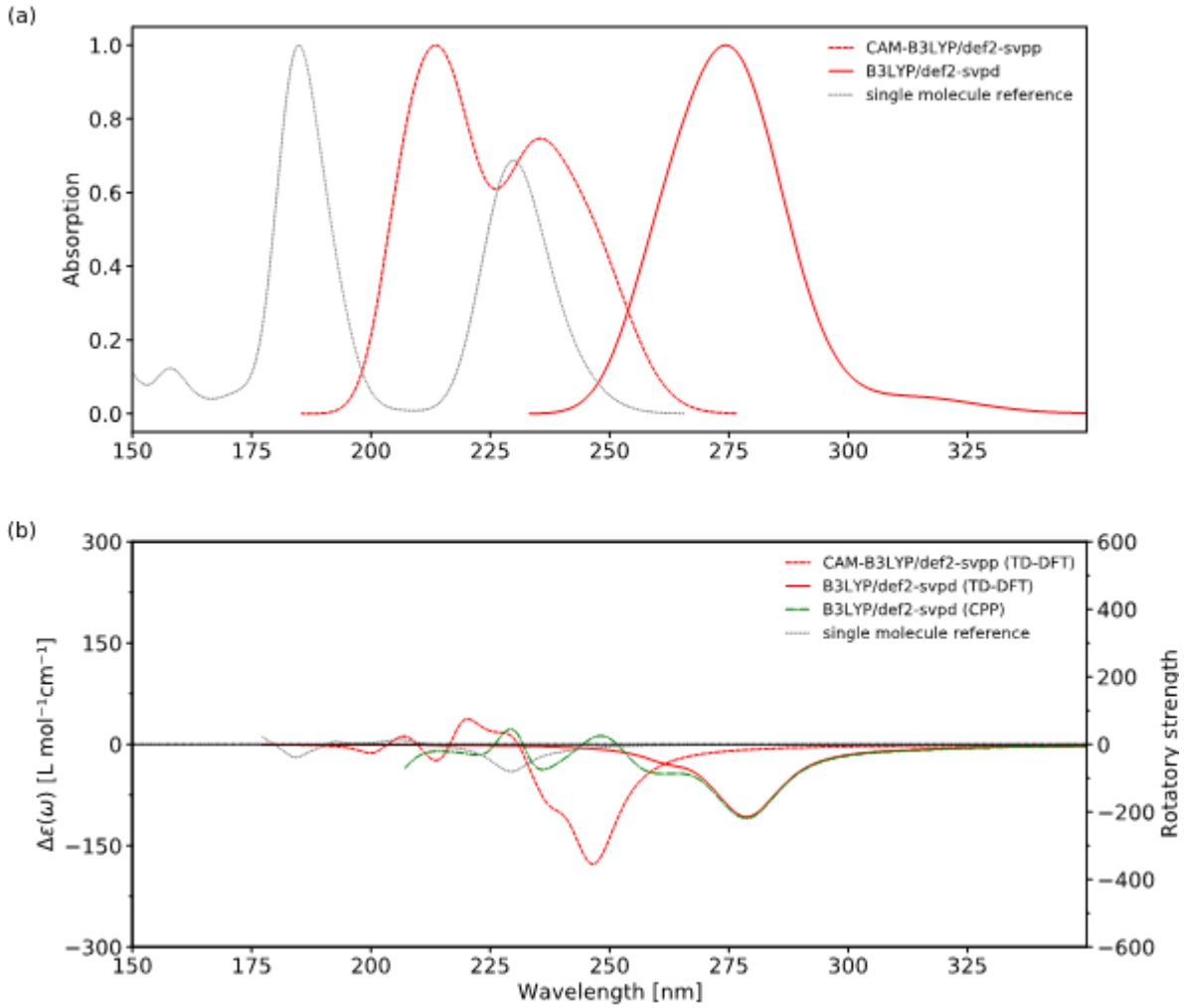

Figure S30. Comparative spectral analysis of dimer using different methods and approaches: panel (a) presents the UV absorption spectra, and panel (b) shows the circular dichroism spectra of the dimer, analyzed using the TDDFT approach for 40 electronic states and the CPP approach focusing on approximately 200-300 nm wavelength range. All spectra are calculated for the dimer in a heptane solvent environment. For comparison, the spectra of a single molecule calculated using the CAM-B3LYP/def2-svpp method in vacuum are also included.

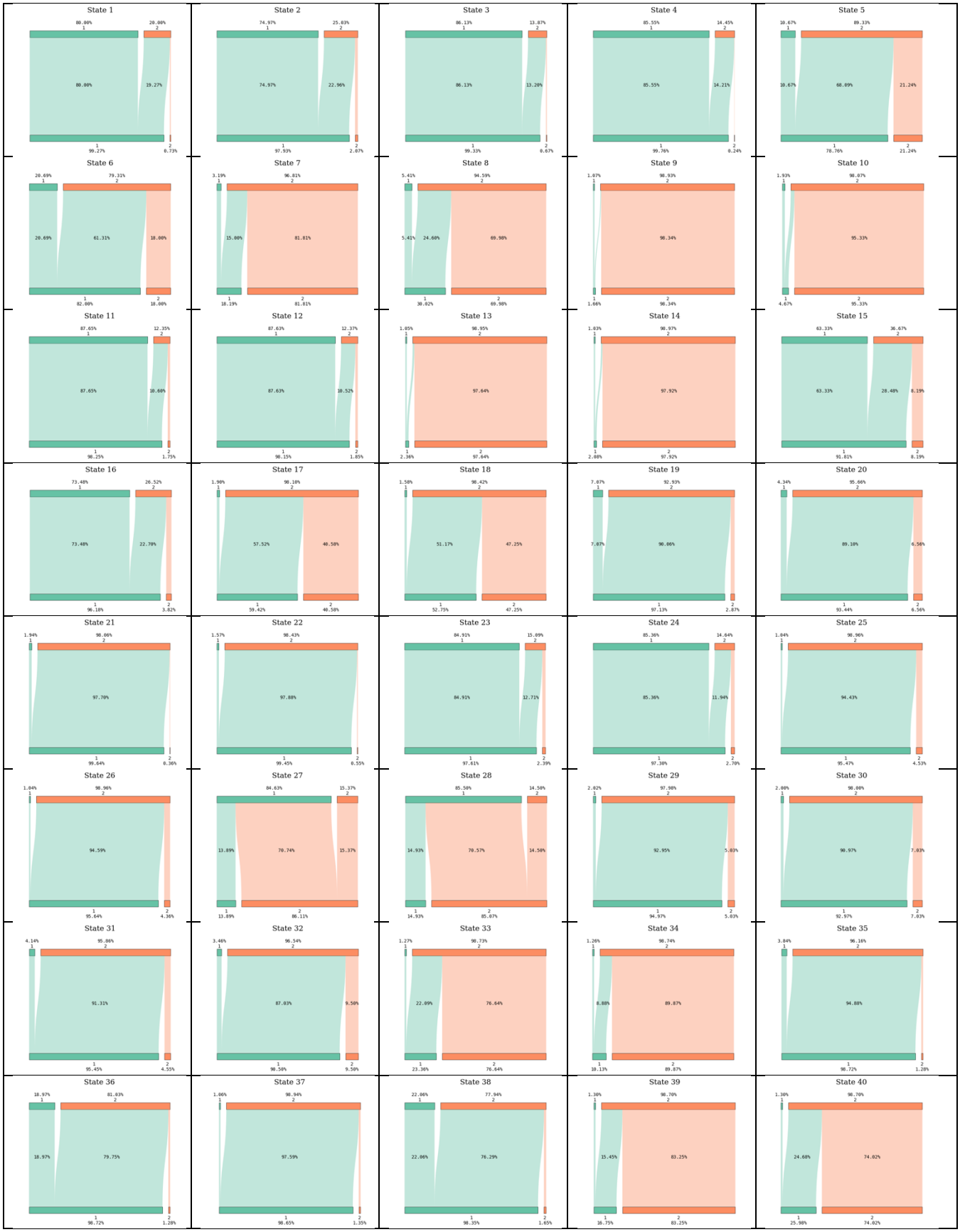

Figure S31. Net electron density transfer between two-layer units composed of 8 (*R*)-SIA molecules across 40 states, as obtained from the VALET analysis tool.

Table S2. Vacuum geometry, CAM-B3LYP/def2-svpp (40 States)

E (eV)	(nm)	(Osc. Str.)	(Rot. Str.)
5.0336	246.31	0.0041	71.0799
5.0364	246.17	0.1039	-344.7848
5.0428	245.87	0.0068	-61.8463
5.0603	245.01	0.0025	-10.4624
5.0836	243.89	0.0009	-28.9620
5.0954	243.33	0.2048	-124.8236
5.1027	242.98	0.0143	-16.2986
5.1047	242.88	0.0135	-61.0947
5.1094	242.66	0.1683	-58.2208
5.1134	242.47	0.0141	-17.5458
5.1414	241.15	0.0184	-121.4318
5.1481	240.83	0.0266	-33.7008
5.1529	240.61	0.0037	-14.3482
5.1533	240.59	0.0190	26.5265
5.1880	238.98	0.4184	447.7763
5.2022	238.33	0.0081	-70.7440
5.2682	235.34	0.0927	-85.8672
5.2706	235.24	0.1387	-95.1585
5.4943	225.66	0.0134	-110.0490
5.5062	225.17	0.0163	-90.9105
5.5703	222.58	0.0218	-18.4189
5.5747	222.41	0.0232	-8.6033
5.6344	220.05	0.2215	105.0278
5.6538	219.30	0.4569	-54.7461
5.7196	216.77	0.0052	70.1069
5.7208	216.72	0.1325	-85.6953
5.7455	215.79	0.0488	9.9810
5.7484	215.68	0.0505	-1.7292
5.7968	213.88	0.0294	-46.2423
5.8097	213.41	0.0234	-54.2614
5.8235	212.90	0.0633	58.9866
5.8312	212.62	0.0949	91.7025
5.8704	211.20	0.0236	11.6576
5.8746	211.05	0.0345	29.6070
6.0145	206.14	0.0004	3.3086
6.0171	206.05	0.0004	5.6483
6.0213	205.91	0.0001	0.5755
6.0284	205.67	0.0006	7.7172
6.0975	203.34	0.0064	0.4893
6.1130	202.82	0.0057	0.6674

Appendix: NMR-spectra of synthesized compounds

(R)-NHMe-SIA

^{1}H NMR

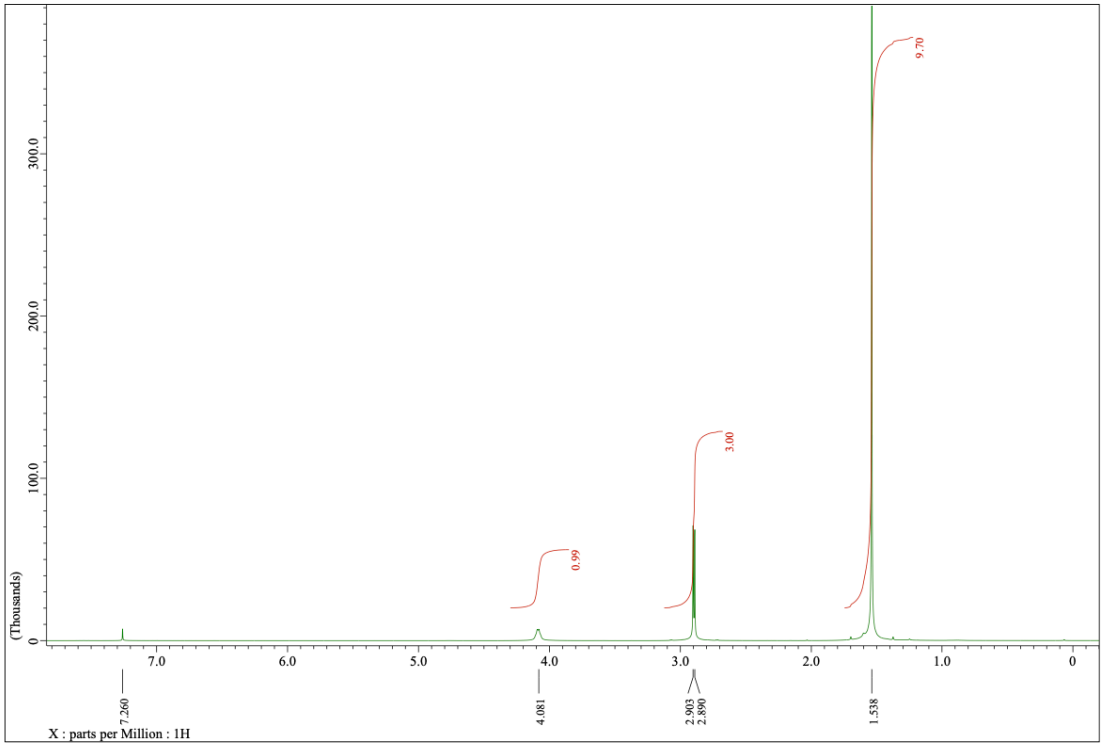

^{13}C NMR

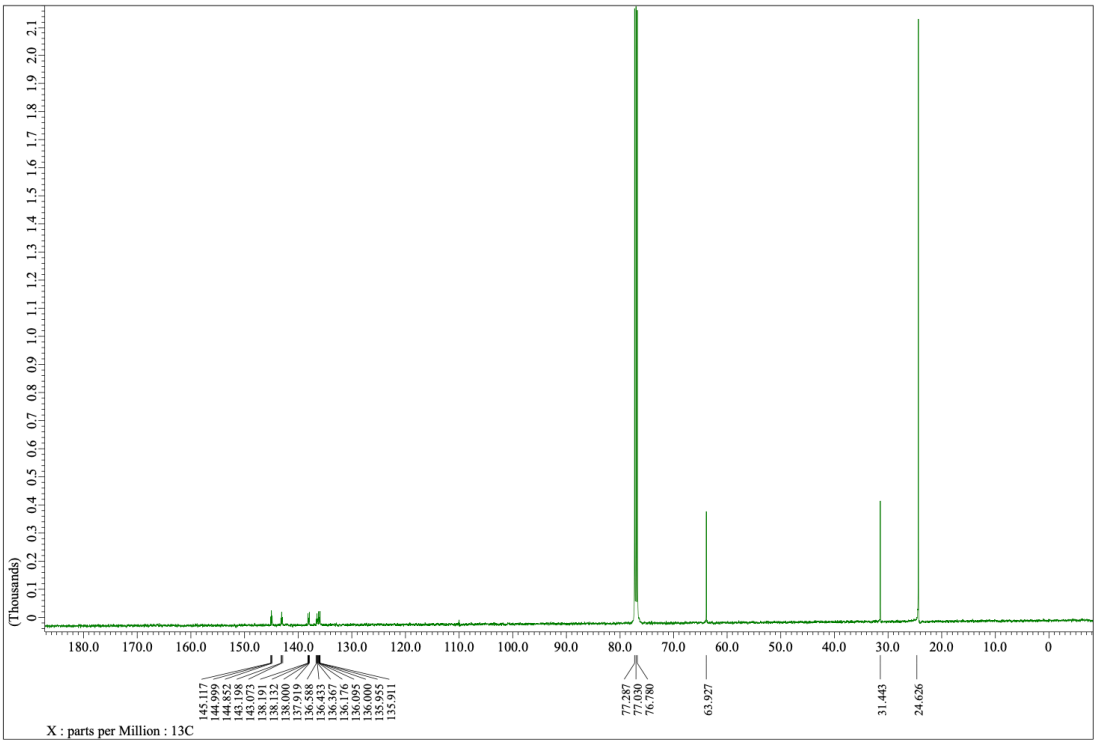

^{19}F NMR

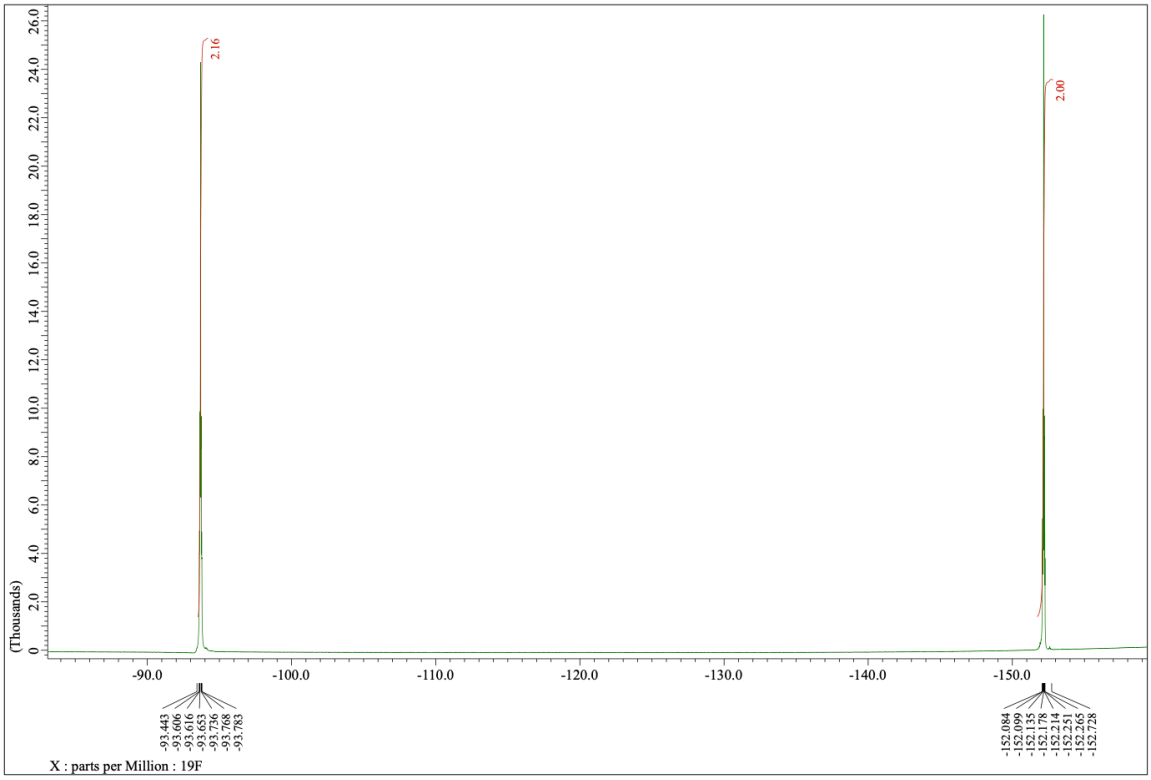

(S)-p-Tol-SIA

^{1}H NMR

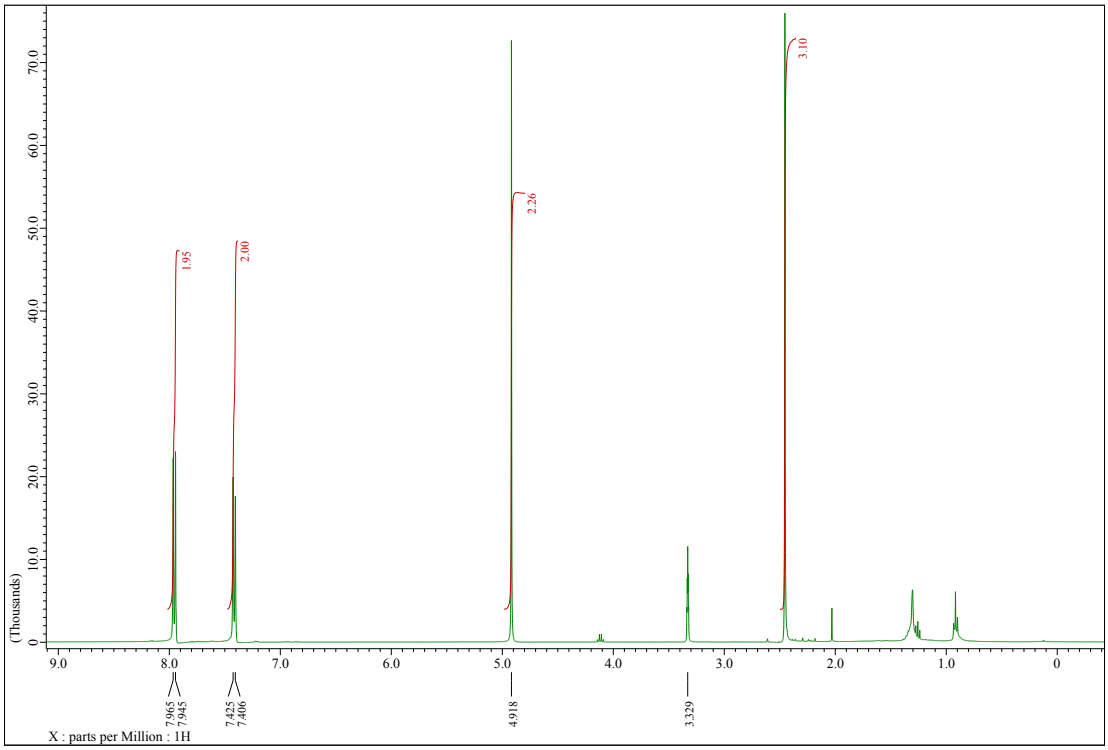

^{13}C NMR

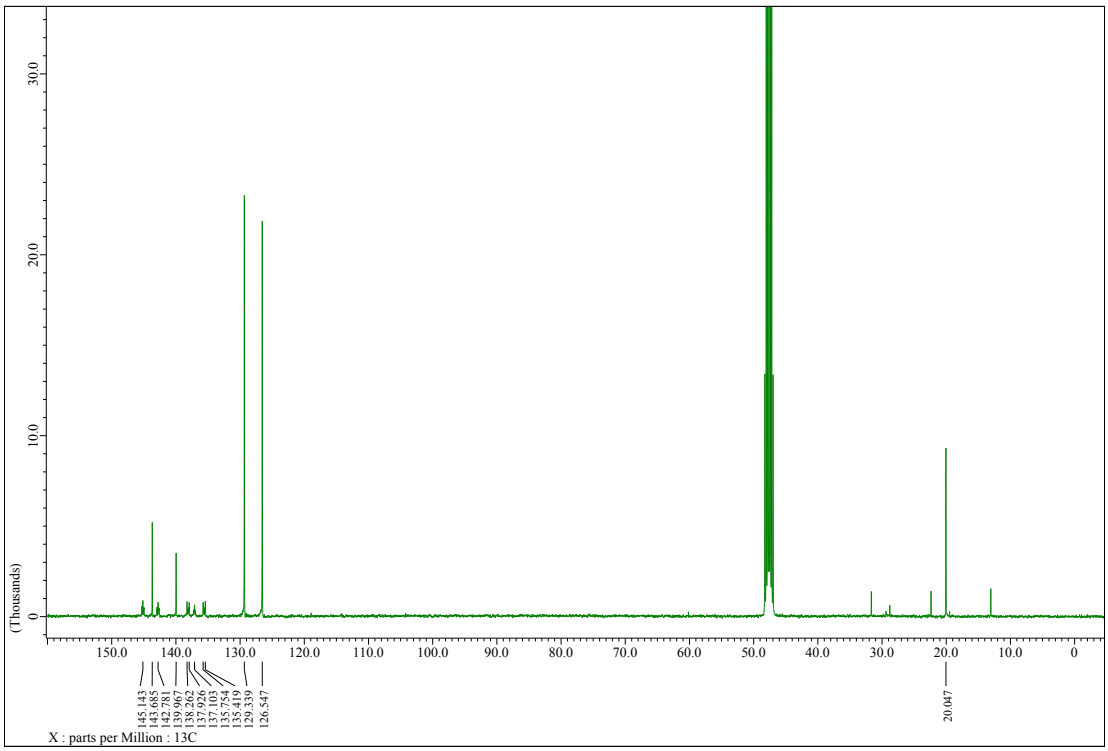

^{19}F NMR

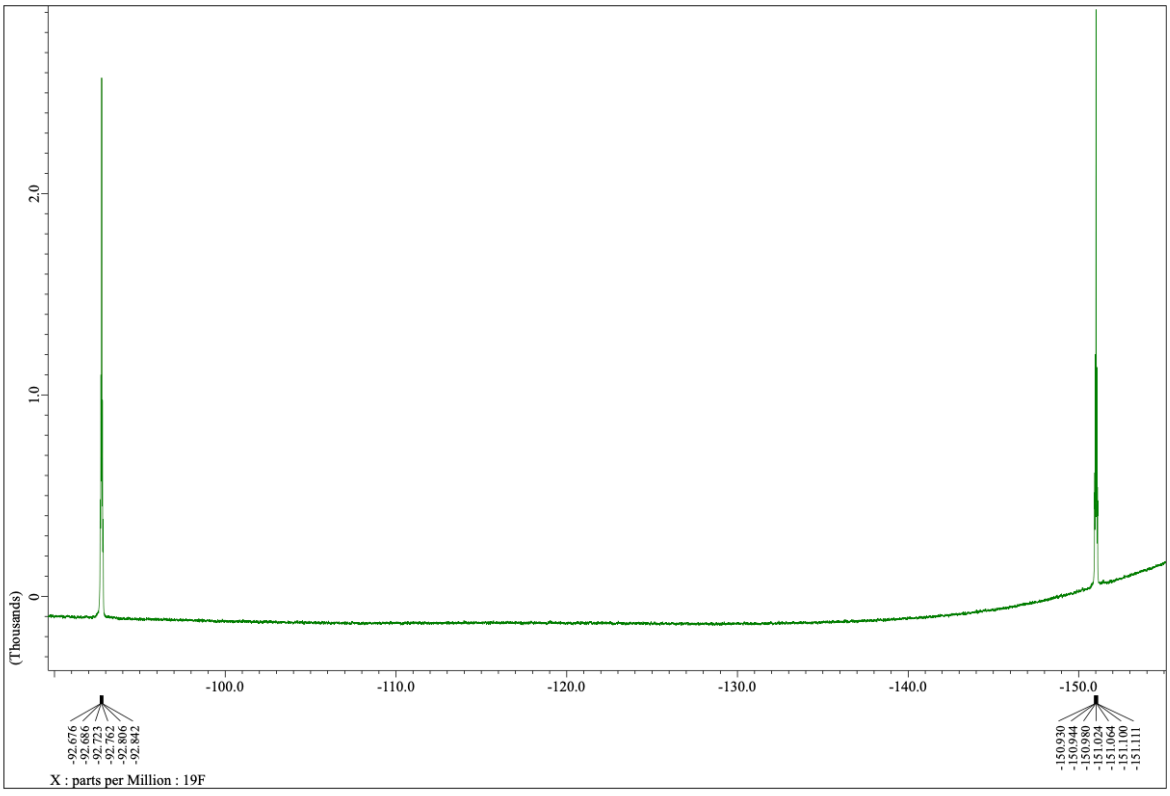

References

1. Frisch, M. J. *et al.* Gaussian 16 Revision C.01. Preprint at (2016).
2. Becke, A. D. Density-Functional Thermochemistry. III. The Role of Exact Exchange. *J. Chem. Phys.* **98**, 5648 (1993).
3. Lee, C., Yang, W. & Parr, R. G. Development of the Colle-Salvetti correlation-energy formula into a functional of the electron density. *Phys. Rev. B* **37**, 785–789 (1988).
4. Stephens, P. J., Devlin, F. J., Chabalowski, C. F. & Frisch, M. J. Ab Initio Calculation of Vibrational Absorption and Circular Dichroism Spectra Using Density Functional Force Fields. *J. Phys. Chem.* **98**, 11623–11627 (1994).
5. Dunning, T. H. Gaussian Basis Sets for use in Correlated Molecular Calculations. I. The Atoms Boron Through Neon and Hydrogen. *J. Chem. Phys.* **90**, 1007–1023 (1989).
6. Wang, J., Wang, W., Kollman, P. A. & Case, D. A. Automatic atom type and bond type perception in molecular mechanical calculations. *J. Mol. Graph Model.* **25**, 247–260 (2006).
7. Wang, J., Wolf, R. M., Caldwell, J. W., Kollman, P. A. & Case, D. A. Development and testing of a general amber force field. *J. Comput. Chem.* **25**, 1157–1174 (2004).
8. Bayly, C. I., Cieplak, P., Cornell, W. & Kollman, P. A. A well-behaved electrostatic potential based method using charge restraints for deriving atomic charges: the RESP model. *J. Phys. Chem.* **97**, 10269–10280 (1993).
9. Yanai, T., Tew, D. P. & Handy, N. C. A new hybrid exchange–correlation functional using the Coulomb-attenuating method (CAM-B3LYP). *Chem. Phys. Lett* **393**, 51–57 (2004).
10. Aidas, K. *et al.* The Dalton Quantum Chemistry Program system. *Wiley Interdiscip. Rev. Comput. Mol. Sci.* **4**, 269–284 (2014).
11. van der Spoel, D. *et al.* GROMACS: Fast, flexible, and free. *J. Comput. Chem.* **26**, 1701–1718 (2005).
12. Hess, B., Kutzner, C., van der Spoel, D. & Lindahl, E. GROMACS 4: Algorithms for Highly Efficient, Load-Balanced, and Scalable Molecular Simulation. *J. Chem. Theory Comput.* **4**, 435–447 (2008).
13. Berendsen, H. J. C., van der Spoel, D., van Drunen, R. GROMACS: A message-passing parallel molecular dynamics implementation. *Comput. Phys. Commun.* **91**, 43–56 (1995).
14. Lindahl, E., Hess, B. & van der Spoel, D. GROMACS 3.0: a package for molecular simulation and trajectory analysis. *Molecular modeling annual* **7**, 306–317 (2001).
15. Darden, T., York, D. & Pedersen, L. Particle mesh Ewald: An N log(N) method for Ewald sums in large systems. *J Chem Phys* **98**, 10089–10092 (1993).
16. Waskom, M. L. seaborn: statistical data visualization. *J Open Source Softw.* **6**, 3021 (2021).
17. Rinkevicius, Z. *et al.* VeloxChem: A Python-driven density-functional theory program for spectroscopy simulations in high-performance computing environments. *Wiley Interdiscip Rev Comput, Mol, Sci,* **10**, e1457 (2020).
18. Jiemchooroj, A., Norman, P. Electronic circular dichroism spectra from the complex polarization propagator. *J. Chem. Phys.*, *126*(13), 134102 (2007). https://doi.org/10.1063/1.2716660
19. Norman, P., Bishop, D. M., Jensen, H. J. Aa., & Oddershede, J.. Near-resonant absorption in the time-dependent self-consistent field and multiconfigurational self-consistent field approximations. *J. Chem. Phys.*, *115*(22), 10323 (2001). https://doi.org/10.1063/1.1415081
20. Norman, P., Bishop, D. M., Jensen, H. J. A., & Oddershede, J.. Nonlinear response theory with relaxation: The first-order hyperpolarizability. *J. Chem. Phys.*, *123*(19), 1–18 (2005). https://doi.org/10.1063/1.2107627

21. Norman, P. (2011). A perspective on nonresonant and resonant electronic response theory for time-dependent molecular properties. *Phys. Chem. Chem. Phys.*, *13*(46), 20519. https://doi.org/10.1039/c1cp21951k